Cell-type specific projection patterns promote balanced activity in cortical microcircuits

Anno C. Kurth[1,2*†], Jasper Albers[1,2*†], Markus Diesmann[1,3,4,5], Sacha J. van Albada[1,6]

[1]Institute for Advanced Simulation (IAS-6), Jülich Research Centre, Jülich, Germany. [2]RWTH Aachen University, Aachen, Germany. [3]JARA-Institut Brain Structure-Function Relationships (INM-10), Jülich Research Centre, Jülich, Germany. [4]Department of Psychiatry, Psychotherapy and Psychosomatics, School of Medicine, RWTH Aachen University, Aachen, Germany. [5]Department of Physics, Faculty 1, RWTH Aachen University, Aachen, Germany. [6]Institute of Zoology, University of Cologne, Cologne, Germany.

[*]These authors contributed equally to this work.
[†] a.kurth@fz-juelich.de, j.albers@fz-juelich.de

Brain structure provides the stage on which activity unfolds. Models linking connectivity to dynamics have relied on probabilistic estimates of connectivity derived from paired electrophysiological recordings or single-neuron morphologies obtained by light microscopy (LM) studies. Only recently have electron microscopy (EM) data sets been processed and made available for volumes of cortex on the cubic millimeter scale, thereby exposing the actual connectivity of neurons. Here, we construct a population-based, layer-resolved connectivity map from EM data, taking into account the spatial scale of local cortical connectivity. We compare the obtained connectivity with a map based on an established LM data set. Simulating spiking neural networks constrained by the derived microcircuit architectures shows that both models allow for biologically plausible ongoing activity when synaptic currents caused by neurons outside the network model are adjusted for every population independently. However, differentially varying the external current onto excitatory and inhibitory populations uncovers that only the EM-based model robustly shows plausible dynamics. Our work confirms the long-standing hypothesis that a preference of excitatory neurons for inhibitory targets, not present in the LM-based model, promotes balanced activity in the cortical microcircuit.

Keywords: local cortical circuitry, electron microscopy, neuroanatomy, structure-dynamics relationship

1 Introduction

Microcircuits are the fundamental building blocks of the neocortex. Early observations identified a vertical compartmentalization into six layers [1] that, as a simplified concept, is still upheld to this day [2]. Horizontally, a modular organization consisting of repeating, stereotyped columns was suggested [3]. These concepts culminated in the notion of the "canonical microcircuit" that tries to reconcile the perceived generic structure of the neocortex with its function [4, 5]. The validity of this notion is subject to debate [6, 7] due to prominent non-uniformities in the composition of cortical tissue across species and areas within one species [8, 9]. Nonetheless, the universal aspects of the area-specific microcircuits constrain cortical dynamics which ultimately underlie their function and thus are of fundamental importance for our understanding of the mammalian brain.

Single instances of local cortical circuits have been reconstructed experimentally [4, 10, 11, 12], and their dynamics and information processing capabilities have been investigated theoretically [4, 13, 14, 15, 16, 17]. Their architecture is usually represented by a connectivity map specifying the probability for two neurons to establish a connection. These maps reduce the complicated circuitry to simple relations between cell types. While this approach neglects higher-order features like connectivity motifs [18, 19, 20], it enables investigations of the links between structural principles of local circuits and their dynamics. While downscaling the numbers of neurons and synapses distorts dynamical predictions [21], networks at realistic neuron and synapse counts provide a means to represent cortical dynamics including correlations faithfully.

Recent years have seen significant advances in the application of electron microscopy (EM) in neuroanatomy [22]. In particular, the adult networks for both sexes of *Caenorhabditis elegans* [23] and large volumes for *Drosophila melanogaster* [24, 25] have been fully reconstructed. In mammals, the wiring diagrams for a $0.0005\,\mathrm{mm}^3$ volume of mouse barrel cortex layer 4 [26] and for layer 2/3 pyramidal cells in a $0.003\,\mathrm{mm}^3$ volume of mouse primary visual cortex [27] were uncovered. Recently, Sievers et al. [12] obtained the full connectivity of all neurons in one barrel column of mouse barrel cortex containing about ten thousand neurons in a volume of roughly $0.2\,\mathrm{mm}^3$ of cortical tissue.

Combining advanced EM imagery with novel machine learning and data processing techniques recently enabled the reconstruction of local cortical networks in unprecedented detail at the cubic millimeter scale for mouse visual cortex [28] and human temporal cortex [29] handling petabytes of raw data. These reconstructions allow a more thorough look into the architecture of local cortical circuits beyond single columns than was previously possible. Due to technical limitations, the resulting con-

nectomes are not complete: since axons require extensive manual proofreading, only a fraction of all synapses can be fully traced back to their source neurons. Consequently, a probabilistic description of connectivity is still needed.

In this study, we investigate the implications of newly obtained EM-based reconstructions for cortical modeling. To this end, we derive a layer-resolved, population-based connectivity map from the subset of proofread neurons in a $\sim 1\,\mathrm{mm}^3$ EM reconstruction of mouse visual cortex [28]. As a reference, we compare with a model based on established light microscopy (LM) data [10] which we devise according to identical principles. Leveraging the explanatory power of the balanced random network paradigm [30, 31], we simulate spiking neural networks based on the two connectivity maps. Their comparison explores implications of connectivity structure in the form of cell-type-specific projection patterns for neuronal activity. Preliminary results have been presented in abstract form [32].

2 Results

To construct the microcircuit models, we first need to estimate the spatial range of local cortical connectivity between populations. This estimate is used to constrain the model sizes. Given these sizes, we determine probabilistic connectivity maps describing the local cortical circuitry. Finally, we perform spiking neural network simulations of the two models and link their dynamics back to their structure.

Binzegger et al. [10] estimate connectivity based on light-microscopic morphological reconstructions of 39 neurons from cat primary visual cortex, using a generalized version of Peters' rule [33, 34]. Supplementing the data with previously obtained numbers of neurons and synapses [35, 36], the authors provide estimates for the numbers of synapses between neurons of various classes. For inhibitory neurons, the authors mainly focus on basket cells, leaving a certain fraction of inhibitory synapses unexplained.

The MICrONS data set [28] contains an EM reconstruction of $\sim 1\,\mathrm{mm}^3$ of mouse visual cortex, consisting of about 75 thousand neurons and about 500 million synapses. For this work, we only consider connections originating from 266 presynaptic neurons with fully reconstructed and proofread axons.

While the MICrONS data give direct access to *actual* neural connections, the data of Binzegger et al. [10] yield *potential* connectivity. In the following, we denote the model based on the MICrONS data set with $\mathcal{M}_{EM}$, and the model based on the Binzegger data set with $\mathcal{M}_{LM}$. In the two models, the cortical layers 2/3, 4, 5, and 6 are distinguished (henceforth, we refer to these as L2/3, L4, L5, and L6). Each layer contains one excitatory (E) and two inhibitory populations (Ib, Inb) corresponding to basket and non-basket cells. For the LM data set, we follow Izhikevich and Edelman [37], assigning unexplained inhibitory synapses to presynaptic non-basket cells. In the EM data set, all neurons can be straightforwardly mapped to one of the populations.

2.1 Spatial connectivity

We estimate the spatial organization of local cortical connections using both the distance-dependent mean number of synapses and the distance-dependent connection probability. Here, the connection probability is defined as the probability that two neurons establish at least one synapse. The connection probability consequently neglects the multiplicity of synapses between pairs of neurons.

We assume an exponential decay of the mean number of synapses $S_{AB}(d)$ between one presynaptic neuron of population B and one postsynaptic neuron of population A with horizontal somatic distance d:

$$S_{AB}(d) = S^0_{AB} \exp\left(-\frac{d}{\lambda^{\mathrm{syn}}_{AB}}\right) \tag{1}$$

Here, S^0_{AB} denotes the peak number of synapses, and $\lambda^{\mathrm{syn}}_{AB}$ denotes the characteristic length of cortical connectivity between populations B and A. Taking the density $\omega(d)$ of distances d between pre- and postsynaptic neurons into account, the density of the expected mean number of synapses $s_{AB}(d)$ between a single neuron in presynaptic population B and all neurons in postsynaptic population A at distance d is $\omega(d) \cdot S_{AB}(d)$.

Likewise, we assume an exponential decay of the connection probability with distance d between individual neurons in the presynaptic population B and postsynaptic population A:

$$p_{AB}(d) = p^0_{AB} \exp\left(-\frac{d}{\lambda^{\mathrm{conn}}_{AB}}\right) \tag{2}$$

Here, p^0_{AB} denotes the connection probability at zero distance. $p_{AB}(d)$ is the conditional probability for a neuron in population B to form at least one synapse with a particular neuron in population A given that the horizontal distance of their somata is d.

For $\mathcal{M}_{EM}$, $S_{AB}(d)$ and $p_{AB}(d)$ can straightforwardly be extracted from the actual connectivity reported in the EM data. Figure 1a shows example fits of the density of the mean number of synapses, with resulting spatial decay constants $\lambda^{\mathrm{syn}}_{AB}$ displayed in Figure 1A. We here assume a uniform distribution of neurons to approximate the true distribution of distances in the reconstructed volume, avoiding problems arising due to sparse data for some population pairs. (cf. Section 4.1). Further, we show example fits for the connection probability in Figure 1b and spatial decay constants $\lambda^{\mathrm{conn}}_{AB}$ in Figure 1B. In agreement with the literature, we find that the spatial scales of local excitatory and inhibitory connectivity at the studied range are generally comparable, with a tendency for excitatory connection lengths to exceed the inhibitory ones [39, 40, 41, 19]. Furthermore, we observe that $S_{AB}(d)$ consistently exhibits smaller characteristic lengths than $p_{AB}(d)$. Calculating the fraction

$$c_X = \frac{\lambda^{\mathrm{syn}}_{A,vX}}{\lambda^{\mathrm{conn}}_{A,vX}} \quad , \quad X \in \{\mathrm{E}, \mathrm{Ib}, \mathrm{Inb}\} \tag{3}$$

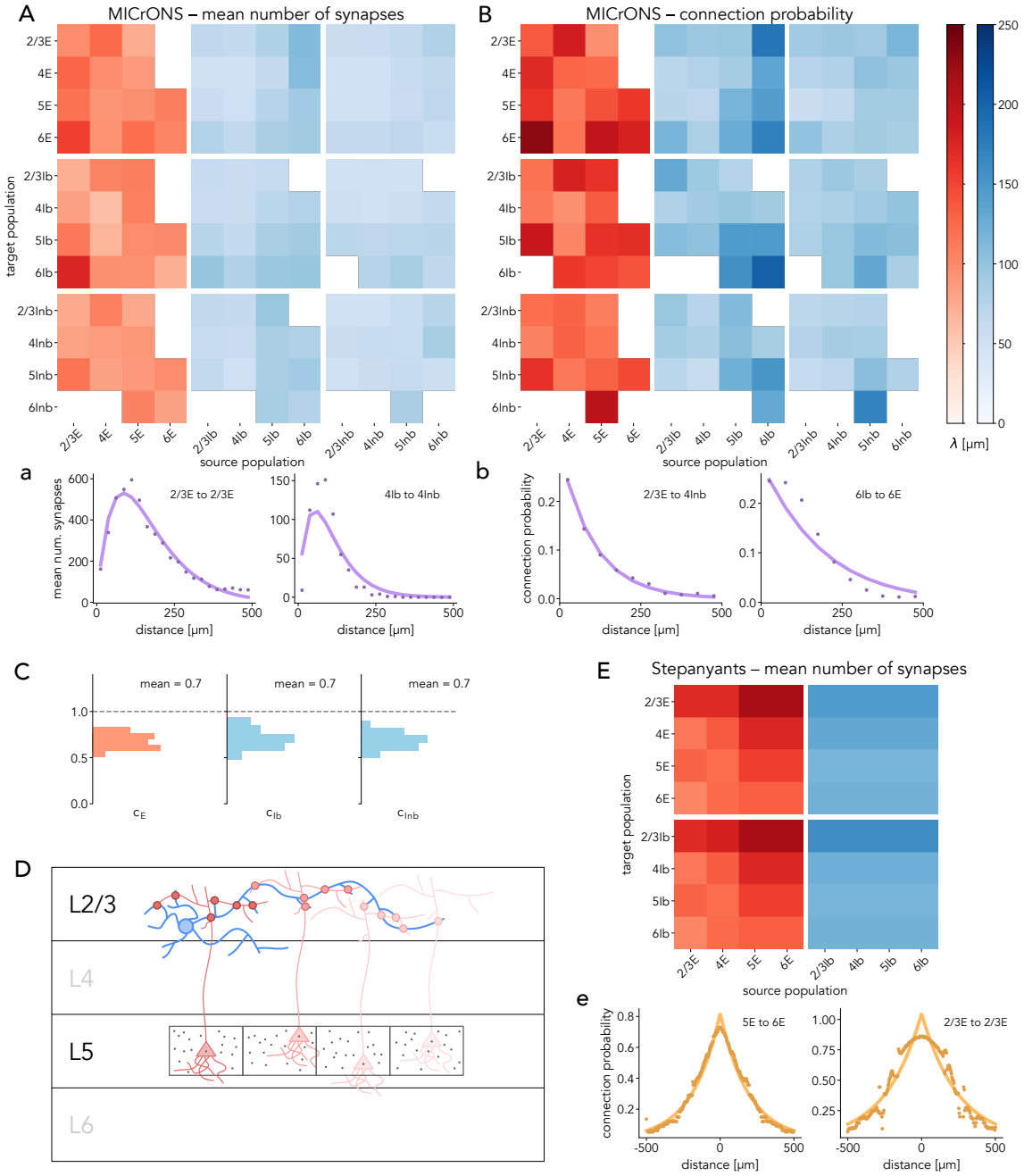

Figure 1: **Spatial scale of actual and potential connectivity for the mean number of synapses and the connection probability. A** Spatial scale of the mean number of synapses estimated from MICrONS data. Rows and columns organized according to population (E: excitatory, Ib: inhibitory basket, Inb: inhibitory non-basket) and cortical layer (2/3, 4, 5, 6). Colors in water tap notation: shades of red indicate excitatory, shades of blue inhibitory connections. White tiles indicate < 50 synapses. **B** Spatial scale of the connection probability estimated from EM data (actual connectivity). Same representation as in A. **C** Ratios between spatial scales of the mean number of synapses and the connection probability for actual connectivity from the EM data set. Histogram over all pairs of populations. **D** Illustration of calculation of potential connectivity from morphologies based on Peters' rule. Location of presynaptic neuron (blue) of population B fixed. Postsynaptic neuron (red) of population A randomly placed in a box with side length $\Delta = 25\,\mu\text{m}$ centered at horizontal position of presynaptic and original vertical coordinate of postsynaptic neuron. Position and rotation around vertical axis sampled $n = 100$ times (gray dots). Connection probability defined as m/n where m is the number of samples for which axon and dendrite are sufficiently close (red circles) at least once. **E** Spatial scale of the mean number of synapses estimated from data by Stepanyants et al. [38]. Excitatory-to-excitatory characteristic lengths estimated from connection probabilities and converted using $c^\star$. Remaining length scales estimated from expected number of potential synapses. Same color code as in A, B. **a,b,e** Example fits showcasing high-quality (left) and low-quality (right) curve fits (see Section S1.1 for overview of fits).

for all pairs of populations, where v is the layer of the presynaptic population and X is that population's cell type, we observe a consistent average $c^\star = 0.7$ (Figure 1C). Thereby, we can estimate $\lambda_{AB}^{\text{syn}}$ from $\lambda_{AB}^{\text{conn}}$, and vice versa.

For $\mathcal{M}_{LM}$, data on actual connectivity is not available. Instead, the spatial scale of the potential connectivity has been estimated solely based on the morphological reconstructions [38, 42]: a potential synapse between a pre- and postsynaptic neuron is registered if their axon and dendrite are sufficiently close (Figure 1D). With this approach, the authors estimate both the mean number of synapses and the connection probability. First, we assess the consistency of the LM potential connectivity with that from the EM data set. Using the provided morphologies, we reproduce the method (Figure 1D) to obtain an estimate of $\lambda_{AB}^{\text{conn,pot}}$ from potential connectivity. Comparing to the previously derived estimates from actual connectivity, $\lambda_{AB}^{\text{conn}}$, we find a good agreement across most pairs of populations (Figure S5).

Next, we calculate $\lambda_{AB}^{\text{syn,pot}}$ for all pairs of populations. In this methodology, we expect that the estimated number of potential synapses is prone to noise due to multiple adjacent segments of reconstructed neural processes being counted as locations of potential synapses. Thus, we use estimates of the connection probability for the pairings of populations where this information is available in [38], and then convert $\lambda_{AB}^{\text{conn,pot}}$ to $\lambda_{AB}^{\text{syn,pot}}$ using $c^\star$. For all other pairs of populations, we directly estimate $S_{AB}(d)$. For pairs of populations with no data in [38], we make additional generalizing assumptions (Section S1.2). Example fits of this procedure are shown in Figure 1e, with the resulting $\lambda_{AB}^{\text{syn,pot}}$ displayed in Figure 1E.

2.2 Connectivity maps

Because our models $\mathcal{M}_{LM}$ and $\mathcal{M}_{EM}$ consider distance-independent mean connection probabilities p_{AB}, the size of the represented cortical tissue and consequently the number of neurons and synapses must be fixed to derive the corresponding connectivity maps. To this end, we distribute neurons with realistic densities for each model in a template space. Assuming the distance-dependence of the mean number of synapses Equation 1, we determine the fraction of model-internal synapses for each pair of pre- and postsynaptic populations for circular patches of cortical tissue (Figure 2A). Here, model-internal synapses refer to incoming synapses originating from neurons in the model. The model radii $r_{EM}^\star$ and $r_{LM}^\star$ are then chosen such that the fractions of model-internal synapses averaged over pre- and postsynaptic populations are approximately 75 % (see Section 4.2), resulting in $r_{EM}^\star = 0.55\,\text{mm}$ and $r_{LM}^\star = 0.75\,\text{mm}$.

We observe that $\mathcal{M}_{LM}$ has a higher number of neurons in most populations, which is expected due to the larger size of the model. Turning to connectivity, we observe that the populations of $\mathcal{M}_{LM}$ have a significantly higher in-degree, i.e., number of incoming connections per neuron, except for 6Ib (Figure 2B). Consequently, the connection probabilities between populations are higher in $\mathcal{M}_{LM}$ than in $\mathcal{M}_{EM}$ (Figure 2C). Still, common patterns can be identified: both models show an excitatory sub-circuit between L2/3E and L5E, inhibitory basket cells project mainly within the same layer, and inhibitory non-basket cells preferentially target neurons in the same or higher layers. The main differences can be observed in the projection pattern of excitatory to inhibitory cells, as further discussed in Section 2.4.

2.3 Model dynamics

To investigate the dynamical properties of the constructed models $\mathcal{M}_{LM}$ and $\mathcal{M}_{EM}$, we instantiate and simulate spiking neural networks defined by the derived numbers of neurons and connectivity maps (see Section 4.3). Neurons are modeled as leaky integrate-and-fire units with conductance-based synapses using the neural simulation engine `NEST` [43]. Excitatory and inhibitory non-basket cells are modeled as regular-spiking neurons and include spike-frequency adaptation and relative refractoriness [44]; inhibitory basket cells, which are PV-expressing, are fast-spiking neurons and are modeled without adaptation [45] (see Section 4.3). We constrain the recurrent synaptic weights using the data of Avermann et al. [46] for E, Ib, and Inb neurons of layer 2/3 in rat cortex. While this choice neglects layer- and species-specific diversity, it reduces model complexity. The weights are consistent with a recently discussed hierarchy of connection strengths in mouse visual cortex [47] (see Section S1.3). Synaptic inputs from neurons not contained in the networks are modeled as excitatory conductance fluctuations in the form of Ornstein-Uhlenbeck processes with population-specific mean μ_A, variance σ_A, and time scale τ_A [48, 49]. The extrinsic drive to each neuron is statistically independent of all other drives. For a detailed model specification see Section S1.4.

The extrinsic drive to both network models is adjusted to approximately satisfy experimentally observed firing rates [50, 51] using the method suggested by Isbister et al. [49] (Table 7, Table 8). Concretely, μ_A and σ_A are chosen for each population A such that $\sigma_A = \chi\mu_A$ with cell-type independent χ. In the resultant state, the spiking activity of both networks exhibits biologically plausible characteristics: asynchronous irregular activity [52, 53] (Figure 3A,B), low firing rates obeying $\nu_{\text{Ib}} > \nu_{\text{Inb}} > \nu_{\text{E}}$ in most cases [54, 55, 56] (Figure 3C,F), broadly distributed coefficients of variation of the inter-spike intervals [57] (Figure 3D,G), and low synchrony assessed by co-fluctuations of neural membrane potentials [58] (Figure 3E,H). The dot displays only include neurons that spiked at least once in the observation interval, akin to experimental recordings where silent neurons remain unobserved.

To systematically investigate the dynamical repertoire of both models, we perform a parameter scan varying the mean drives μ_E and μ_I to the sets of excitatory and inhibitory populations. We find that $\mathcal{M}_{LM}$ has only a narrow band of extrinsic drives for which the firing rates resemble experimentally observed activity: if μ_I is too large, the excitatory cells do not fire or have a

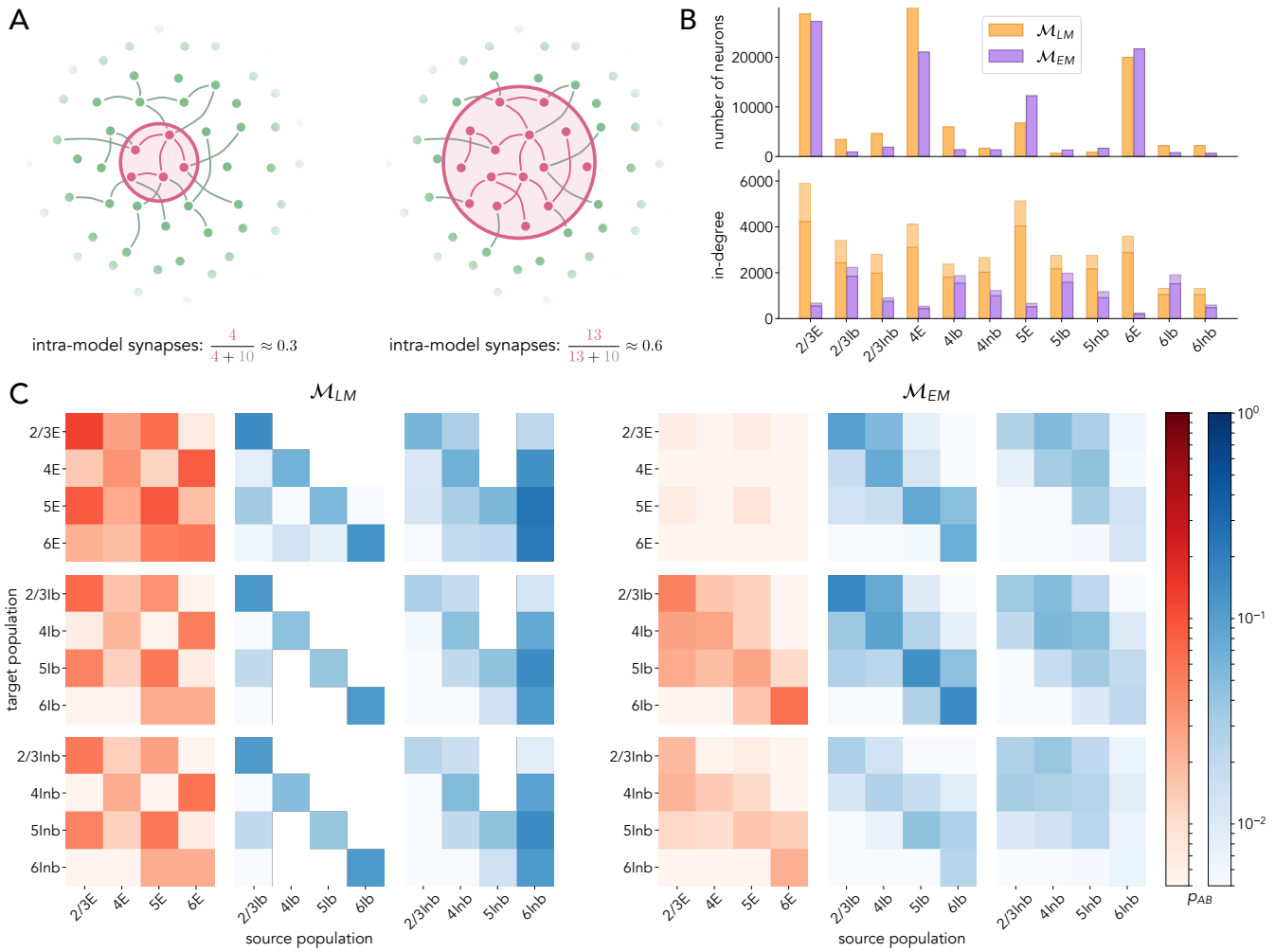

Figure 2: **Model construction and connectivity maps.** **A** Sketch illustrating the fraction of intra-model synapses depending on model size. **B** Numbers of neurons (top) and in-degrees (bottom) for both models with radii $r^{\star}_{EM} = 0.55\,\text{mm}$ and $r^{\star}_{LM} = 0.75\,\text{mm}$. The model radii are chosen so that the fraction of model-internal synapses is approximately 75 % averaged over population pairs (Equation 5). For the in-degrees, solid bars indicate the number of intra-model synapses, while transparent bars (stacked) indicate synapses with presynaptic neurons not contained in the models. $\mathcal{M}_{EM}$ consists of ∼96 thousand neurons and ∼64 million synapses; $\mathcal{M}_{LM}$ consists of ∼108 thousand neurons and ∼455 million synapses. **C** Mean number of synapses between two arbitrary neurons of given source- and target populations (same representation as in Figure 1A).

vanishingly small firing rate, and if μ_E is too large, the network rapidly transitions to a highly synchronized state (Figure 4A-E left). In contrast, the activity of $\mathcal{M}_{EM}$ smoothly depends on the extrinsic drive with plausible firing rates, irregular spiking, and low synchrony across a large domain of the parameter space (Figure 4A-E right). Additionally, $\mathcal{M}_{EM}$ exhibits the paradoxical effect [59, 60, 61], where increasing μ_I decreases the firing rate of inhibitory basket cells. Note that also for $\mathcal{M}_{LM}$ the inhibitory basket cells reduce their firing rate when increasing μ_I for large μ_E and small μ_I. We do not consider this as a paradoxical effect, since for large μ_E and small μ_I, $\mathcal{M}_{LM}$ exhibits biologically implausible, highly synchronized activity, suggesting that in this case, the reduced inhibitory firing rate is due to a qualitative change in dynamical state.

2.4 Linking structure and dynamics

What is the structural reason for this discrepancy between the models? Consider the specificity of projections from a given source population to excitatory versus inhibitory neurons in a target layer, which we term *target specificity* [14] (cf. Equation 10). The target specificity attains a positive (negative) value if a projection preferentially targets excitatory (inhibitory) neurons (Figure 5). For $\mathcal{M}_{LM}$, all presynaptic populations have a positive target specificity. For $\mathcal{M}_{EM}$, a more nuanced picture emerges where excitatory presynaptic populations preferentially target inhibitory neurons while there are inhibitory neurons of both cell types with positive as well as negative target specificities. This suggests that excitatory neurons that are more strongly innervated by recurrent connections, as is the case in $\mathcal{M}_{LM}$, are the origin of pathological dynam-

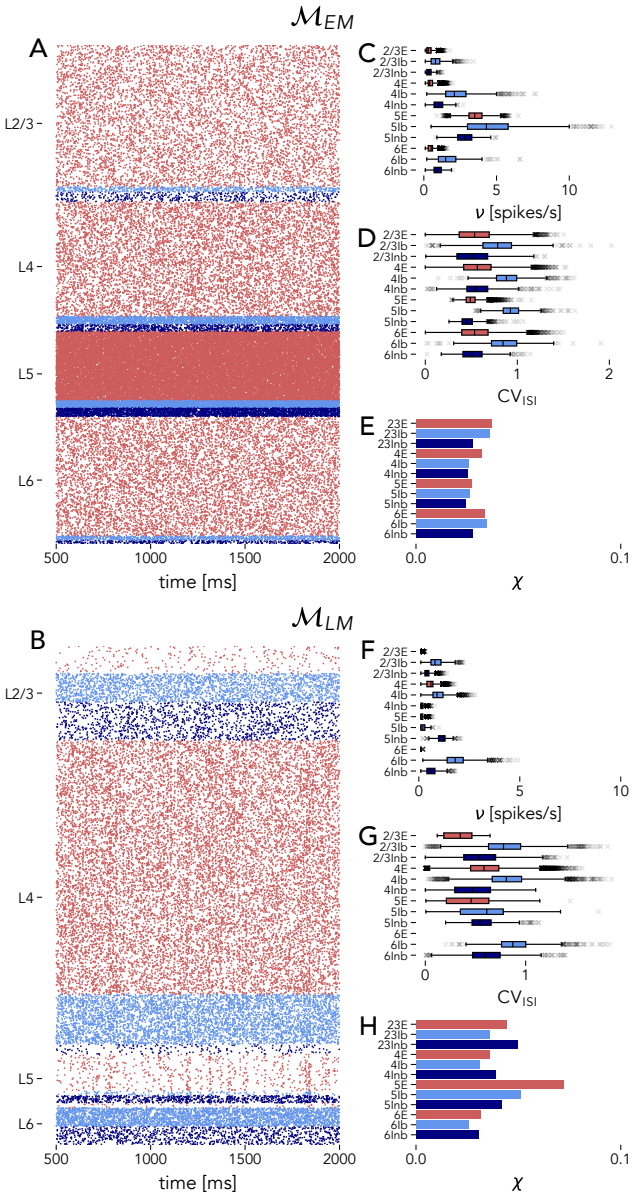

Figure 3: **Model activity with optimized external input.** Red indicates excitatory, light blue inhibitory basket, and dark blue inhibitory non-basket populations. The simulation gathers statistics over 10 s of biological time starting 0.5 s after simulation onset. **A, B** Raster plots (spikes marked as dots) of 50% of neurons that spiked at least once for the time stretch from 0.5 s to 2.0 s. **C–H** Population-resolved firing rates ν, coefficients of variation of the inter-spike interval CV_{ISI} (Equation 8), and synchrony χ (Equation 9).

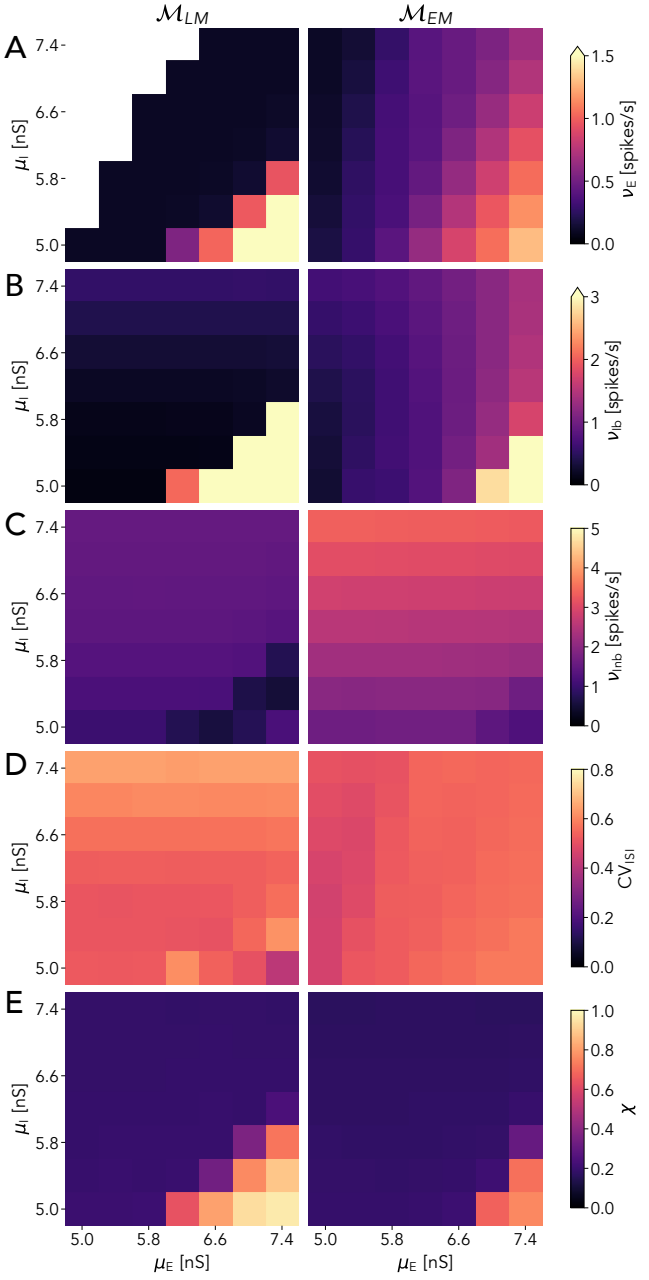

Figure 4: **Model activity under variation of extrinsic drive.** Simulation time of $T = 10$ s with a simulation period of $T_{pre} = 0.5$ s before data acquisition to avoid transients due to initial conditions. The mean input to all excitatory (μ_E) and inhibitory (μ_I) neurons is varied. Arrow at the top of color bars indicates that higher values are assigned the color of the maximum value. **A-C** Population-averaged firing rates of E, Ib, and Inb neurons. **D** Population-averaged coefficients of variation CV_{ISI} of the inter-spike interval (Equation 8). **E** Population-averaged synchrony χ (Equation 9).

ics. We test this in $\mathcal{M}_{EM}$ by redistributing synapses from excitatory neurons that previously targeted inhibitory neurons such that they target excitatory neurons instead. This procedure conserves the total number of synapses. When a moderate number of synapses are redistributed, the target specificity of excitatory neurons becomes balanced (Figure 6A, left). The resulting model retains the biologically plausible dynamics across a large part of the parameter space (Figure 6B-F, left column). Increasing the number of synapses that are redistributed until the target specificity of excitatory neurons resembles that of $\mathcal{M}_{LM}$ (Figure 6A, right), $\mathcal{M}_{EM}$ shows qualitatively similar dynamics to $\mathcal{M}_{LM}$ (Figure 6B-F, right column):

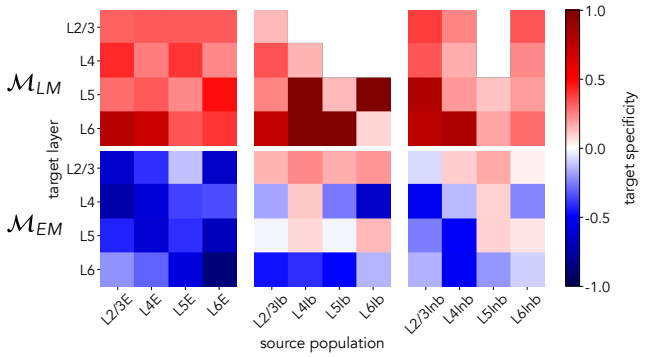

Figure 5: **Target specificity for both network models.** Positive values indicate a preferential targeting of excitatory neurons in a layer by a given source population; negative values indicate preference for inhibitory targets.

for excitatory neurons, the transition between the firing regime at large μ_E and small μ_I and that at smaller μ_E and large μ_I becomes more abrupt. Further, the paradoxical effect in the activity of inhibitory neurons becomes less pronounced. Finally, the increased target specificity results in highly synchronous activity for a larger portion of the parameter space.

Thus, the biologically implausible activity of $\mathcal{M}_{LM}$ can in part be explained by the underlying positive target specificity, which in turn stems from the assumptions of the reconstruction of the local cortical circuit.

3 Discussion

In the present work, we revisit local cortical microcircuit architectures. Based on two reconstruction techniques—light microscopy (LM) and electron microscopy (EM)—we compare cortical connectivity and study implications for cortical dynamics using spiking neural network models. Our results show that strong recurrent innervation of excitatory neurons leads to pathological dynamics in the LM-based model. Consequently, the LM-based connectivity needs to be modified to allow for biologically plausible activity over a wide range of input parameters. Conversely, the EM-based model exhibits balanced, biologically plausible activity for a wide range of extrinsic drives without the need for further modifications. This can be understood in terms of the target specificity: excitatory neurons preferentially target inhibitory ones, while inhibitory neurons have a diverse targeting pattern.

Such layer-specific projection patterns are in agreement with the study by Potjans and Diesmann [14] who amended connectivity derived from Binzegger et al. [10] with physiological connectivity data from several species and cortical areas, motivated by a discrepancy in target specificity between data sources (see their Figures 4 and S3). This reorganization leads to a stronger targeting of inhibitory neurons in certain layers by excitatory neurons, which is essential for asynchronous and irregular

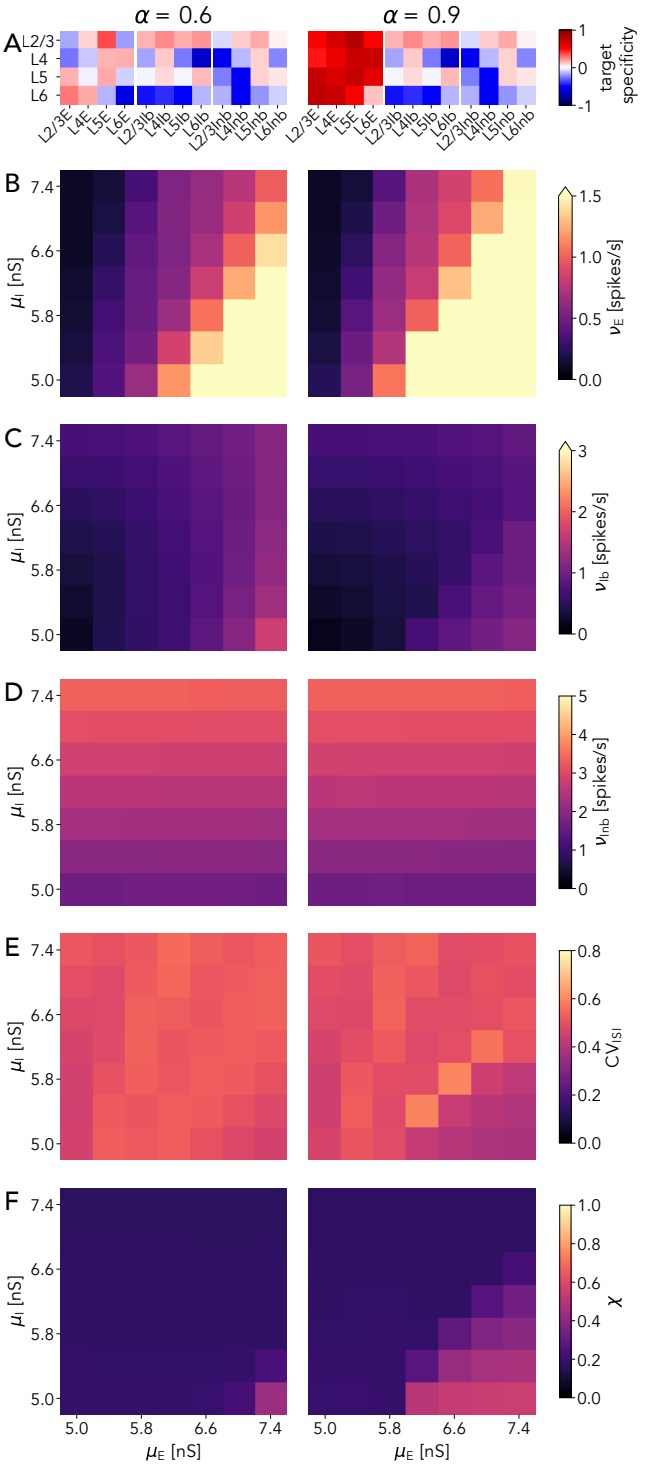

Figure 6: **Effect of increased target specificity in $\mathcal{M}_{EM}$.** Parameter $\alpha \in [0, 1]$ linearly controls redistribution of synapses onto excitatory neurons leading to an increase in target specificity (cf. Section 4.5). $\alpha = 0$ corresponds to the original model, $\alpha = 1$ implies that all synapses target excitatory neurons. Color code in top panels as in Figure 5, in bottom panels as in Figure 4.

activity with realistic firing rates. Our results confirm the hypothesized negative target specificity of especially excitatory projections using reconstructions from a single

brain.

3.1 Modeling paradigm

The approach to modeling neural circuits employed here rests on the seminal insights from balanced random networks [30, 31, 62]. These networks have since been extended to multiple populations taking into account biological details such as the cell-type specific organization of cortex [14, 63], multiple inhibitory populations [63, 64, 65], or morphologically detailed neuron models [15, 49] to study cortical dynamics and function. Here, for the first time, we present a random network model constrained by EM-based connectivity data. While derived from a specific connectome, the obtained probabilistic connectivity rules represent the general connectivity of a template mouse visual cortex and allow for efficient instantiations of neural network models in distributed computers [66]. As such, they are amendable by future EM reconstructions and provide a starting point for generic cortex modeling. Using the derived characteristic spatial extents of connectivity, the model can be promoted to a spatially organized network that is scalable to sizes beyond the local cortical circuit. Such networks exhibit rich dynamics across space [67, 68, 69] and enable investigations of, for example, activity and function in visual cortical areas [16, 17, 70].

Alternatively, bio-realistic modeling can be based on the specific, completely reconstructed circuitry of one animal. In terms of mammalian local circuits spanning all layers, these data are only available for one column of mouse barrel cortex [12]. Advanced laboratories combine physiological measurements of the activity of a piece of tissue with a subsequent EM reconstruction, allowing for self-consistent investigations of the relationship between the structure, dynamics, and function in a particular brain (e.g. MICrONS Consortium et al. [28]). In contrast, the abstractions employed in the probabilistic approach put forward here expose principles of cortical architecture and processing.

3.2 Spatial decay of connection probability and mean number of synapses

Different spatial scales of local cortical connectivity in mouse visual cortex and cat V1 (Figure 1A, E) are not surprising given interspecies differences. However, also the methodologies used to determine the decay of connection probability with distance differ between the data sets. While LM data only allow estimating the potential connectivity, the EM data allow deriving the spatial extent of actual connectivity based on established synapses and accurate neuron positions as well as potential connectivity from the provided morphologies. Comparing the two methodologies for deriving the distance-dependent connection probabilities from the EM data set (Figure S5), we find a general agreement between the estimates of characteristic length scales.

Further, using the detailed information provided by the EM data, we compare the spatial decay of connection probability to that of the mean number of synapses. For both quantities, we assume an exponential decay with distance, which provides accurate estimates for a wide range of pre- and postsynaptic pairs of populations (Figure S1, Figure S2). We show that the mean number of synapses exhibits a decay with a consistently shorter characteristic length for all considered pairs of populations (Figure 1C). The reason for this difference may be that synapses between a given pair of neurons 'beget' more synapses, leading to long-tailed distributions of synaptic multiplicity [71]. Numbers of neuron pairs with high synaptic multiplicity would then fall off faster with distance than numbers of neuron pairs with low synaptic multiplicity, causing the observed difference in spatial decay between connection probability and the mean number of synapses.

The exponential model for the connection probability with distance (Equation 2) is in agreement with the experimental data as well (Figure S3). For distances above about 100 µm, Markov et al. [72] suggest an exponential decay for the fraction of labeled neurons from retrograde tracing. This finding is consistent with our results, whether fractions of labeled neurons are more reflective of numbers of synapses or of connection probabilities, since both follow an exponential decay with distance.

3.3 Target specificity controls dynamical repertoire

Instantiating and simulating spiking neural network models based on the derived connectivity maps and spatial scales, we find that both the EM- and LM-based models can exhibit biologically plausible activity (Figure 3). However, varying the background drive to excitatory and inhibitory populations systematically reveals that $\mathcal{M}_{LM}$ only behaves in a biologically plausible way for a narrow band of the parameter space: the model is prone to completely silent excitatory populations or network-wide strong, pathological oscillations. In contrast, $\mathcal{M}_{EM}$ is well-behaved across a wider range of drive parameters, a necessary prerequisite for robust cortical computation. Furthermore, $\mathcal{M}_{EM}$ reproduces the experimentally observed paradoxical effect for inhibitory neurons [60].

The differences in dynamical behavior between the two models are explained by cell-type-specific targeting patterns. Our results indicate that a strong preference of excitatory populations for targeting excitatory populations leads to biologically implausible activity: for $\mathcal{M}_{LM}$, the aforementioned targeting pattern is observed (Figure 5); redistributing synapses in $\mathcal{M}_{EM}$ to match the targeting pattern of $\mathcal{M}_{LM}$ leads to qualitatively similar dynamics (Figure 6).

3.4 Conclusion

In this work, we provide openly accessible connectivity maps and models of the cortical microcircuit based on established LM and recent EM reconstructions. As such, the obtained maps and models provide platforms

for future modeling studies of local cortical networks. Possible extensions include taking into account more detailed single-neuron parameters and connection weights, multapse distributions, higher-order connectivity motifs, distance-dependent connectivity, functionally specific external input, neuronal morphologies, and functional properties such as plasticity.

Both models, $\mathcal{M}_{LM}$ and $\mathcal{M}_{EM}$, reduce the intricate morphology and complex response patterns of nerve cells to leaky integrate-and-fire point neuron models with conductance-based synapses and, in the case of excitatory cells and inhibitory non-basket cells, two adaptation currents. Given this level of description, the EM-based model outperforms the LM-based model in terms of biological plausibility of the emerging activity due to differences in cell-type-specific targeting patterns. This suggests that the EM-based connectivity is to be preferred as a starting point in future modeling of local cortical circuits. Our study confirms by the analysis of direct anatomical measurements the prediction of the existence of a negative target specificity of excitatory projections realized in the microcircuit model of Potjans and Diesmann [14].

4 Methods

4.1 Spatial connectivity

To obtain estimates for the characteristic lengths of local cortical connectivity, we assume an exponential decay for the mean number of synapses with lateral distance between somata (Equation 1). The EM reconstruction allows for determining the density of the mean number of actual synapses $s_{AB}(d)$ between a single presynaptic proofread neuron and all postsynaptic neurons at inter-somatic distance d for pairs of the considered cell types. Using the distribution of uniformly sampled points in a rectangle with distance d [73], we approximate the number of potential postsynaptic partners $\omega(d)$ given the dimensions of the reconstructed volume. We then fit

$$s_{AB}(d) = S^0_{AB} \cdot \omega(d) \cdot \exp\left(-d/\lambda^{\text{syn}}_{AB}\right) \tag{4}$$

to obtain λ_{AB} between presynaptic population B and postsynaptic population A.

Additionally, we estimate the distance-dependent connection probability, i.e., the probability of establishing at least one synapse. We define the connection probability $p_{AB}(d_1, d_2)$ between a presynaptic neuron of population B and a postsynaptic neuron of population A that have a horizontal inter-somatic distance d with $d_1 \leq d \leq d_2$ as the number of connected neuron pairs divided by the total number of neuron pairs in the same range of distances. Here, the total number of neuron pairs is given by the product of the number of neurons of populations A and B within the range of distances. We also assume an exponential decay for the continuous $p_{AB}(d)$, albeit with a different characteristic length scale (Equation 2). The quantity $c^\star = \langle \frac{\lambda^{\text{syn}}_{AB}}{\lambda^{\text{conn}}_{AB}} \rangle_{AB}$ measures the discrepancy between the distance dependence of the mean number of synapses and the connection probability based on the EM data set.

For the LM data set, Stepanyants et al. [38] derive the connection probability using potential connectivity, defined as the probability that a source and target neuron of given cell types at inter-somatic distance d form at least one synapse based on morphological reconstructions of single neurons. This connection probability is given for a subset of pairs of populations. For these, we again fit Equation 2, which we convert to an estimate of the characteristic length of the mean number of synapses $\lambda^{\text{syn}}_{AB}$ using $c^\star$. For a different subset of pairs of populations, Stepanyants et al. [38] derive the distance-dependent mean number of synapses $S_{AB}(d)$ under further assumptions, which we fit using Equation 1 to also obtain $\lambda^{\text{syn}}_{AB}$. These fits are displayed in Figure S4. Finally, for pairs of populations in our model where Stepanyants et al. [38] provide neither of the two quantities, we generalize from the existing estimates as detailed in Section S1.2.

Further, we assess the consistency of the LM potential connectivity with the potential and actual connectivity from the EM data. For this, we use the same morphology-based ansatz to derive a connection probability based on potential connectivity from the EM data. Compared to [38], we use more single-cell reconstructions (266 compared to 41), and fewer cell positions within each box (100 compared to 1000). Then, we compare the resulting length scales of spatial connectivity with estimates from the actual connectivity derived above. For the EM data set, the two methodologies result in estimates of $\lambda^{\text{conn}}_{AB}$ that are comparable across all pairs of populations.

In all cases, `scipy.optimize.curve_fit` [74] performs non-linear least-squares fits using the Levenberg-Marquardt algorithm [75].

4.2 Connectivity maps

To constrain the size of the models, we calculate

$$F(r) = \langle F_{AB}(r) \rangle_{AB} = \left\langle \frac{S^{\text{int},\leq r}_{AB}}{S^{\text{total},\leq r}_{AB}} \right\rangle , \tag{5}$$

the fraction of intra-model synapses for a circular patch of cortex with radius r. To determine the expected number of synapses from population B to population A of neurons within a circular patch with radius r, $S^{\text{int},\leq r}_{AB}$, we uniformly distribute neurons with realistic densities in the patch and calculate the number of synapses according to Equation 1. Similarly, the total number of synapses between the populations, $S^{\text{total},\leq r}_{AB}$, is determined by increasing the sampling radius of the presynaptic population to $3r$. The model radius $r^\star$ for both models is determined so that $F(r^\star) \approx 75\%$.

We calculate the number of synapses between populations A and B internal to the model as

$$S^{\text{int}}_{AB} = \pi r^{\star 2} \cdot \rho^S_{AB} \cdot F_{AB}(r^\star) ,$$

where ρ^S_{AB} is the density of synapses from population B to population A extracted from the respective data set, and

finally the distance-independent connection probability between a neuron in presynaptic population B and a neuron in postsynaptic population A as

$$p_{AB} = \frac{S^{\text{int}}_{AB}}{N_A N_B}$$

where N_A, N_B are the number of neurons in populations A and B, respectively.

Population pairs having insufficient data to constrain the characteristic length scales (cf. S2) are neglected in determining the model sizes, but they are nevertheless connected according to the (scaled) total number of synapses in the respective data sets. Thus, also populations without a fitted length scale are connected, unless the corresponding number of reported synapses is zero.

4.3 Network model and single-neuron dynamics

Using the derived connectivity maps we instantiate network graphs for the two models using a pairwise Bernoulli connection rule with source- and target-population-specific connection probabilities p_{AB} (see the user-level documentation of NEST for an ontology based on [76]). The resulting networks are directed versions of Erdős-Rényi graphs [77].

Single neurons are modeled as leaky integrate-and-fire units with conductance-based synapses. The membrane potential for units representing inhibitory basket cells evolves as

$$\begin{aligned} C_m \dot{V}_m = &- g_L \left(V_m - E_L\right) - \left(g_{\text{ex}} + g_{\text{ext}}\right)\left(V_m - E_{\text{ex}}\right) \\ &- g_{\text{in}} \left(V_m - E_{\text{in}}\right) \end{aligned} \tag{6}$$

with the membrane capacitance C_m, leak conductance g_L and reversal potentials $E_L, E_{\text{ex}}, E_{\text{in}}$. The conductances obey

$$\begin{aligned} \tau_{\text{ex}} \dot{g_{\text{ex}}}(t) &= -g_{\text{ex}}(t) + \tau_{\text{ex}} \sum_j w_j \sum_{t_j} \delta(t - t_j - d_j) \\ \tau_{\text{in}} \dot{g_{\text{in}}}(t) &= -g_{\text{in}}(t) + \tau_{\text{in}} \sum_k w_k \sum_{t_k} \delta(t - t_k - d_k) \\ \tau_{\text{ext}} \dot{g_{\text{ext}}}(t) &= -(g_{\text{ext}}(t) - \mu) + \sigma\sqrt{2\tau_{\text{ext}}}\eta(t) \ , \end{aligned}$$

where j (k) is a presynaptic neuron, t_j (t_k) its spike times, w_j (w_k) the weight on a target neuron, d_j (d_k) is the connection delay, $\tau_{\text{ex}}, \tau_{\text{in}}$ are the synaptic time constants, μ is the mean and σ the standard deviation of the extrinsic drive modeled as an Ornstein-Uhlenbeck process (η denotes white noise), and τ_{ext} its timescale. The timescales of response conductances and the extrinsic conductance modulation can differ since the latter entails slower fluctuations from the not explicitly modeled neural tissue. For all simulations, we fix $\sigma/\mu = \xi = 0.2$ [48] while the mean varies between populations and experiments. If V_m crosses the threshold V_{th} at time t', the unit emits a spike with this time-stamp, is reset to V_{reset}, and is kept at this value for τ_{ref}. Units representing excitatory cells or inhibitory non-basket cells have additional currents that implement spike-frequency adaptation (a) and relative refractoriness (rr):

$$\begin{aligned} C_m \dot{V}_m = &-g_L \left(V_m - E_L\right) - \left(g_{\text{ex}} + g_{\text{ext}}\right)\left(V_m - E_{\text{ex}}\right) \\ &- g_{\text{in}} \left(V_m - E_{\text{in}}\right) - g_{\text{a}} \left(V_m - E_{\text{a}}\right) - g_{\text{rr}} \left(V_m - E_{\text{rr}}\right) . \end{aligned} \tag{7}$$

The corresponding conductances evolve according to

$$\begin{aligned} \tau_{\text{a}} \dot{g_{\text{a}}}(t) &= -g_{\text{a}}(t) + \tau_{\text{a}} \sum_{t_i} \delta(t - t_i) \\ \tau_{\text{rr}} \dot{g_{\text{rr}}}(t) &= -g_{\text{rr}}(t) + \tau_{\text{rr}} \sum_{t_i} \delta(t - t_i) \end{aligned}$$

where t_i are the timings of the spikes emitted by the units.

The neuron models used in this study are specified using `NESTML` [78]. The state of the neurons (Equation 6, Equation 7) is integrated with an embedded Runge-Kutta-Fehlberg 4(5) method [79]. The Langevin equation describing the extrinsic drive is integrated using an exact scheme [80, 81].

4.4 Analysis of dynamical data

The firing rates are determined for each neuron by counting the spikes and dividing by the observation time. Coefficients of variation of the inter-spike intervals (ISIs) for each neuron are given by

$$\text{CV}_{\text{ISI}} = \frac{\text{standard deviation of ISIs}}{\text{mean of ISIs}} \ . \tag{8}$$

Both quantities are calculated using the Electrophysiology Analysis Toolkit (`elephant`[82]). To determine the synchrony χ of each population, we record the membrane potential of 50 neurons per population and calculate

$$\chi^2 = \frac{\left\langle \left(\langle V_m \rangle_i - \langle V_m \rangle_{i,T} \right)^2 \right\rangle_T}{\left\langle \left(V_m - \langle V_m \rangle_T \right)^2 \right\rangle_{i,T}} \tag{9}$$

where $\langle ... \rangle_i$ denotes the average over the neurons in one population, and $\langle ... \rangle_T$ denotes the time average.

4.5 Target specificity

For a presynaptic population B and a layer v, the target specificity is given by

$$\text{TS}_{v,B} = \frac{p_{v\text{E},B} - p_{v\text{Ib},B} - p_{v\text{Inb},B}}{p_{v\text{E},B} + p_{v\text{Ib},B} + p_{v\text{Inb},B}} \in [-1, 1] \ . \tag{10}$$

A positive (negative) value indicates that B preferentially targets excitatory (inhibitory) neurons in layer v.

We redistribute synapses between populations to increase the value of the target specificity using a control parameter $\alpha \in [0, 1]$ while keeping the total number of synapses fixed. On the level of the mean number of synapses, this amounts to:

$$\begin{aligned} S^{\text{int},\alpha}_{u\text{Ib},v\text{E}} &= (1 - \alpha) \cdot S^{\text{int}}_{u\text{Ib},v\text{E}} \\ S^{\text{int},\alpha}_{u\text{Inb},v\text{E}} &= (1 - \alpha) \cdot S^{\text{int}}_{u\text{Inb},v\text{E}} \\ S^{\text{int},\alpha}_{u\text{E},v\text{E}} &= S_{v\text{E},v\text{E}} + S^{\text{int}}_{u\text{Ib},v\text{E}} + S^{\text{int}}_{v\text{Inb},v\text{E}} \end{aligned}$$

This definition implies that $\alpha = 0$ leaves the connectivity maps (and thus the target specificity values) unchanged, while for $\alpha = 1$ all synapses exclusively target excitatory populations (TS = 1).

Code and data availability

The data and code to reproduce the results are openly available on Zenodo (https://doi.org/10.5281/zenodo.13886620).

Acknowledgments

This project has received funding from NeuroSys as part of the initiative "Clusters4Future" by the Federal Ministry of Education and Research BMBF (03ZU1106CB), the European Union's Horizon Europe Programme under the Specific Grant Agreement No. 101147319 (EBRAINS 2.0 Project) and the Priority Program (SPP 2041 "Computational Connectomics") of the Deutsche Forschungsgemeinschaft. The authors gratefully acknowledge the computing time granted by the JARA Vergabegremium and provided on the JARA Partition part of the supercomputer JURECA at Forschungszentrum Jülich (computation grant JINB33).

References

[1] K. Brodmann. *Vergleichende Lokalisationslehre der Großhirnrinde in ihren Prinzipien dargestellt auf Grund des Zellenbaues*. Leipzig: Johann Ambrosius Barth, 1909.

[2] K. Zilles and K. Amunts. "Architecture of the Cerebral Cortex". In: *The Human Nervous System*. Ed. by J. K. Mai and G. Paxinos. Third Edition. San Diego: Academic Press, 2012, pp. 836–895.

[3] V. B. Mountcastle. "Modality and topographic properties of single neurons in cat's somatic sensory cortex". *Journal of Neurophysiology* 20.4 (1957), pp. 408–434.

[4] R. J. Douglas, K. A. C. Martin, and D. Whitteridge. "A Canonical Microcircuit for Neocortex". *Neural Computation* 1.4 (1989), pp. 480–488.

[5] R. J. Douglas and K. A. C. Martin. "Neuronal Circuits of the Neocortex". *Annual Review of Neuroscience* 27 (2004), pp. 419–451.

[6] J. C. Horton and D. L. Adams. "The cortical column: a structure without a function". *Philosophical Transactions of the Royal Society B* 360.1456 (2005), pp. 837–862.

[7] N. M. M. Da Costa and K. Martin. "Whose cortical column would that be?" *Frontiers in Neuroanatomy* 4 (2010), p. 1265.

[8] S. Herculano-Houzel, C. Watson, and G. Paxinos. "Distribution of neurons in functional areas of the mouse cerebral cortex reveals quantitatively different cortical zones." *Frontiers in Neuroanatomy* 7 (2013), p. 35.

[9] C. E. Collins et al. "Neuron densities vary across and within cortical areas in primates". *Proceedings of the National Academy of Sciences of the United States of America* 107.36 (2010), pp. 15927–15932.

[10] T. Binzegger, R. J. Douglas, and K. A. C. Martin. "A Quantitative Map of the Circuit of Cat Primary Visual Cortex". *Journal of Neuroscience* 39.24 (2004), pp. 8441–8453.

[11] C. Y. C. Chou et al. "Principles of visual cortex excitatory microcircuit organization". *bioRxiv* (2023), pp. 2023–12.

[12] M. Sievers et al. "Connectomic reconstruction of a cortical column". *BioRxiv* (2024), pp. 2024–03.

[13] S. Haeusler and W. Maass. "A statistical analysis of information-processing properties of lamina-specific cortical microcircuit models." *Cerebral Cortex* 17.1 (2007), pp. 149–162.

[14] T. C. Potjans and M. Diesmann. "The Cell-Type Specific Cortical Microcircuit: Relating Structure and Activity in a Full-Scale Spiking Network Model". *Cerebral Cortex* 24.3 (2014), pp. 785–806.

[15] H. Markram et al. "Reconstruction and simulation of neocortical microcircuitry". *Cell* 163.2 (2015), pp. 456–492.

[16] J. Antolík et al. "A comprehensive data-driven model of cat primary visual cortex". *BioRxiv* (2018).

[17] Y. N. Billeh et al. "Systematic integration of structural and functional data into multi-scale models of mouse primary visual cortex". *Neuron* 106.3 (2020), 388–403.e18.

[18] S. Song et al. "Highly nonrandom features of synaptic connectivity in local cortical circuits". *PLOS Biology* 3.3 (2005), e68.

[19] R. Perin, T. K. Berger, and H. Markram. "A synaptic organizing principle for cortical neuronal groups". *Proceedings of the National Academy of Sciences of the United States of America* 108.13 (2011), pp. 5419–5424.

[20] H. Peng et al. "Morphological diversity of single neurons in molecularly defined cell types". *Nature* 598.7879 (2021), pp. 174–181.

[21] S. J. van Albada, M. Helias, and M. Diesmann. "Scalability of Asynchronous Networks Is Limited by One-to-One Mapping between Effective Connectivity and Correlations". *PLOS Computational Biology* 11.9 (2015). Ed. by P. E. Latham, e1004490.

[22] Y. Kubota, J. Sohn, and Y. Kawaguchi. "Large volume electron microscopy and neural microcircuit analysis". *Frontiers in Neural Circuits* 12 (2018), p. 98.

[23] S. J. Cook et al. "Whole-animal connectomes of both Caenorhabditis elegans sexes". *Nature* 571.7763 (2019), pp. 63–71.

[24] Z. Zheng et al. "A complete electron microscopy volume of the brain of adult Drosophila melanogaster". *Cell* 174.3 (2018), pp. 730–743.

[25] L. K. Scheffer et al. "A connectome and analysis of the adult Drosophila central brain". *eLife* 9 (2020), e57443.

[26] A. Motta et al. "Dense connectomic reconstruction in layer 4 of the somatosensory cortex". *Science* 366.6469 (2019), eaay3134.

[27] S. Dorkenwald et al. "Binary and analog variation of synapses between cortical pyramidal neurons". *eLife* 11 (2022), e76120.

[28] MICrONS Consortium et al. "Functional connectomics spanning multiple areas of mouse visual cortex". *BioRxiv* (2021), pp. 2021–07.

[29] A. Shapson-Coe et al. "A petavoxel fragment of human cerebral cortex reconstructed at nanoscale resolution". *Science* 384.6696 (2024), eadk4858.

[30] C. van Vreeswijk and H. Sompolinsky. "Chaos in Neuronal Networks with Balanced Excitatory and Inhibitory Activity". *Science* 274 (1996), pp. 1724–1726.

[31] D. J. Amit and N. Brunel. "Model of Global Spontaneous Activity and Local Structured Activity During Delay periods in the Cerebral Cortex". *Cerebral Cortex* 7 (1997), pp. 237–252.

[32] A. C. Kurth et al. "Comparing data-driven architecture reconstructions of local cortical circuits". In: *Bernstein Conference 2023*. G-Node, 2023, P 320.

[33] A. Peters and M. L. Feldman. "The projection of the lateral geniculate nucleus to area 17 of the rat cerebral cortex. I. General description." *Journal of Neurocytology* 5.1 (1976), pp. 63–84.

[34] V. Braitenberg and A. Schüz. *Anatomy of the Cortex: Statistics and Geometry*. Berlin, Heidelberg, New York: Springer-Verlag, 1991.

[35] C. Beaulieu and M. Colonnier. "The number of neurons in the different laminae of the binocular and monocular regions of area 17 in the cat". *Journal of Comparative Neurology* 217.3 (1983), pp. 337–344.

[36] C. Beaulieu and M. Colonnier. "A laminar analysis of the number of round-asymmetrical and flat-symmetrical synapses on spines, dendritic trunks, and cell bodies in area 17 of the cat". *Journal of Comparative Neurology* 231 (1985), pp. 180–189.

[37] E. M. Izhikevich and G. M. Edelman. "Large-scale model of mammalian thalamocortical systems". *Proceedings of the National Academy of Sciences of the United States of America* 105.9 (2008), pp. 3593–3598.

[38] A. Stepanyants et al. "Local Potential Connectivity in Cat Primary Visual Cortex". *Cerebral Cortex* 18.1 (2007), pp. 13–28.

[39] R. B. Levy and A. D. Reyes. "Spatial profile of excitatory and inhibitory synaptic connectivity in mouse primary auditory cortex". *Journal of Neuroscience* 32.16 (2012), pp. 5609–5619.

[40] M. W. Reimann et al. "Morphological diversity strongly constrains synaptic connectivity and plasticity". *Cerebral Cortex* 27.9 (2017), pp. 4570–4585.

[41] A. M. Packer and R. Yuste. "Dense, Unspecific Connectivity of Neocortical Parvalbumin-Positive Interneurons: A Canonical Microcircuit for Inhibition?" *Journal of Neuroscience* 31.37 (2011), pp. 13260–13271.

[42] B. Hellwig. "A quantitative analysis of the local connectivity between pyramidal neurons in layers 2/3 of the rat visual cortex". *Biological Cybernetics* 2.82 (2000), pp. 111–121.

[43] M.-O. Gewaltig and M. Diesmann. "NEST (NEural Simulation Tool)". *Scholarpedia Journal* 2.4 (2007), p. 1430.

[44] P. Dayan and L. F. Abbott. *Theoretical Neuroscience*. Cambridge: MIT Press, 2001.

[45] D. Feldmeyer et al. "Inhibitory interneurons and their circuit motifs in the many layers of the barrel cortex". *Neuroscience* 368 (2018), pp. 132–151.

[46] M Avermann et al. "Microcircuits of excitatory and inhibitory neurons in layer 2/3 of mouse barrel cortex". *Journal of Neurophysiology* 107.11 (2012), pp. 3116–3134.

[47] N. Kraynyukova et al. "In vivo extracellular recordings of thalamic and cortical visual responses reveal V1 connectivity rules". *Proceedings of the National Academy of Sciences of the United States of America* 119.41 (2022), e2207032119.

[48] A Destexhe et al. "Fluctuating synaptic conductances recreate in vivo-like activity in neocortical neurons". *Neuroscience* 107.1 (2001), pp. 13–24.

[49] J. B. Isbister et al. "Modeling and Simulation of Neocortical Micro-and Mesocircuitry. Part II: Physiology and Experimentation". *bioRxiv* (2023), pp. 2023–05.

[50] D. L. Ringach, R. M. Shapley, and M. J. Hawken. "Orientation selectivity in macaque V1: diversity and laminar dependence". *Journal of Neuroscience* 22.13 (2002), pp. 5639–5651.

[51] A. Wohrer, M. D. Humphries, and C. K. Machens. "Population-wide distributions of neural activity during perceptual decision-making". *Progress in Neurobiology* 103 (2013), pp. 156–193.

[52] M. R. Cohen and A. Kohn. "Measuring and interpreting neuronal correlations". *Nature Reviews Neuroscience* 14.7 (2011), pp. 811–819.

[53] A. S. Ecker et al. "Decorrelated Neuronal Firing in Cortical Microcircuits". *Science* 327.5965 (2010), pp. 584–587.

[54] A. C. Snyder, M. J. Morais, and M. A. Smith. "Dynamics of excitatory and inhibitory networks are differentially altered by selective attention". *Journal of Neurophysiology* 116.4 (2016), pp. 1807–1820.

[55] B. V. Atallah et al. "Parvalbumin-expressing interneurons linearly transform cortical responses to visual stimuli". *Neuron* 73.1 (2012), pp. 159–170.

[56] L. J. Gentet et al. "Unique functional properties of somatostatin-expressing GABAergic neurons in mouse barrel cortex". *Nature Neuroscience* 15.4 (2012), pp. 607–612.

[57] W. R. Softky and C. Koch. "The Highly Irregular Firing of Cortical Cells Is Inconsistent with Temporal Integration of Random EPSPs". *Journal of Neuroscience* 13.1 (1993), pp. 334–350.

[58] D. Golomb and J. Rinzel. "Clustering in globally coupled inhibitory neurons". *Physica D* 72.3 (1994), pp. 259–282.

[59] M. Tsodyks et al. "Paradoxical effects of external modulation of inhibitory interneurons." *Journal of Neuroscience* 17.11 (1997), pp. 4382–8.

[60] H. Adesnik. "Synaptic mechanisms of feature coding in the visual cortex of awake mice". *Neuron* 95.5 (2017), pp. 1147–1159.

[61] A. Sanzeni et al. "Inhibition stabilization is a widespread property of cortical networks". *eLife* 9 (2020), e54875.

[62] N. Brunel and V. Hakim. "Fast Global Oscillations in Networks of Integrate-and-Fire Neurons with Low Firing Rates". *Neural Computation* 11.7 (1999), pp. 1621–1671.

[63] H.-J. Jiang et al. "A layered microcircuit model of somatosensory cortex with three interneuron types and cell-type-specific short-term plasticity". *Cerebral Cortex* 34.9 (2024), bhae378.

[64] A. Litwin-Kumar, R. Rosenbaum, and B. Doiron. "Inhibitory stabilization and visual coding in cortical circuits with multiple interneuron subtypes". *Journal of Neurophysiology* (2016), jn.00732.2015+.

[65] N. Wagatsuma, S. Nobukawa, and T. Fukai. "A microcircuit model involving parvalbumin, somatostatin, and vasoactive intestinal polypeptide inhibitory interneurons for the modulation of neuronal oscillation during visual processing". *Cerebral Cortex* 33.8 (2023), pp. 4459–4477.

[66] A. Morrison et al. "Advancing the boundaries of high connectivity network simulation with distributed computing". *Neural Computation* 17.8 (2005), pp. 1776–1801.

[67] R. Rosenbaum and B. Doiron. "Balanced Networks of Spiking Neurons with Spatially Dependent Recurrent Connections". *Physical Review X* 4.2 (2014), p. 021039.

[68] R. Pyle and R. Rosenbaum. "Spatiotemporal Dynamics and Reliable Computations in Recurrent Spiking Neural Networks". *Physical Review Letters* 118 (1 2017), p. 018103.

[69] J. Senk et al. "Reconciliation of weak pairwise spike-train correlations and highly coherent local field potentials across space". *ArXiv* (2023), 1805.10235v1 [q–bio.NC].

[70] G. Chen, F. Scherr, and W. Maass. "A data-based large-scale model for primary visual cortex enables brain-like robust and versatile visual processing". *Science Advances* 8.44 (2022), eabq7592.

[71] N. Kasthuri et al. "Saturated reconstruction of a volume of neocortex". *Cell* 162.3 (2015), pp. 648–661.

[72] N. T. Markov et al. "Weight Consistency Specifies Regularities of Macaque Cortical Networks". *Cerebral Cortex* 21.6 (2011), pp. 1254–1272.

[73] T. K. Sheng. "The distance between two random points in plane regions". *Advances in Applied Probability* 17.4 (1985), pp. 748–773.

[74] E. Jones, T. Oliphant, P. Peterson, et al. *SciPy: Open source scientific tools for Python*. 2001.

[75] J. J. Moré. "The Levenberg-Marquardt algorithm: implementation and theory". In: *Numerical analysis: proceedings of the biennial Conference held at Dundee, June 28–July 1, 1977*. Springer. 2006, pp. 105–116.

[76] J. Senk et al. "Connectivity Concepts in Neuronal Network Modeling". *PLOS Computational Biology* 18.9 (2022), e1010086.

[77] P. Erdős and A. Rényi. "On random graphs". *Publicationes Mathematicae* 6 (1959), pp. 290–297.

[78] D. Plotnikov et al. "NESTML: a modeling language for spiking neurons". In: *Modellierung 2016*. Ed. by A. Oberweis and R. Reussner. Vol. P-254. Lecture Notes in Informatics (LNI). Modellierung 2016, Karlsruhe (Germany), 17 Mar 2016 - 19 Mar 2016. Gesellschaft für Informatik e.V. (GI), 2016, pp. 93–108.

[79] E. Fehlberg. *Low-order classical Runge-Kutta formulas with stepsize control and their application to some heat transfer problems*. Vol. 315. National aeronautics and space administration, 1969.

[80] D. T. Gillespie. "Exact numerical simulation of the Ornstein-Uhlenbeck process and its integral". *Physical Review E* 54.2 (1996), pp. 2084–2091.

[81] S. Rotter and M. Diesmann. "Exact digital simulation of time-invariant linear systems with applications to neuronal modeling". *Biological Cybernetics* 81.5-6 (1999), pp. 381–402.

[82] M. Denker et al. *Elephant 0.11.1*. 2022.

S1 Supplementary materials

S1.1 Population-specific characteristic lengths

We fit an exponential decay of the mean number of synapses using Equation 1 and the connection probability using Equation 2 to the actual and potential connectivity derived from EM data to obtain the population-specific characteristic lengths λ_{AB}. Figure S5 compares the length scale of the connection probability obtained from actual and potential connectivity. We find that the two methods produce similar estimates:

$$\gamma_X = \frac{\lambda^{\text{conn}}_{A,vX}}{\lambda^{\text{conn,pot}}_{A,vX}} \approx 1 \quad \forall v, X \tag{11}$$

where v is the layer and X is the cell type of the presynaptic population.

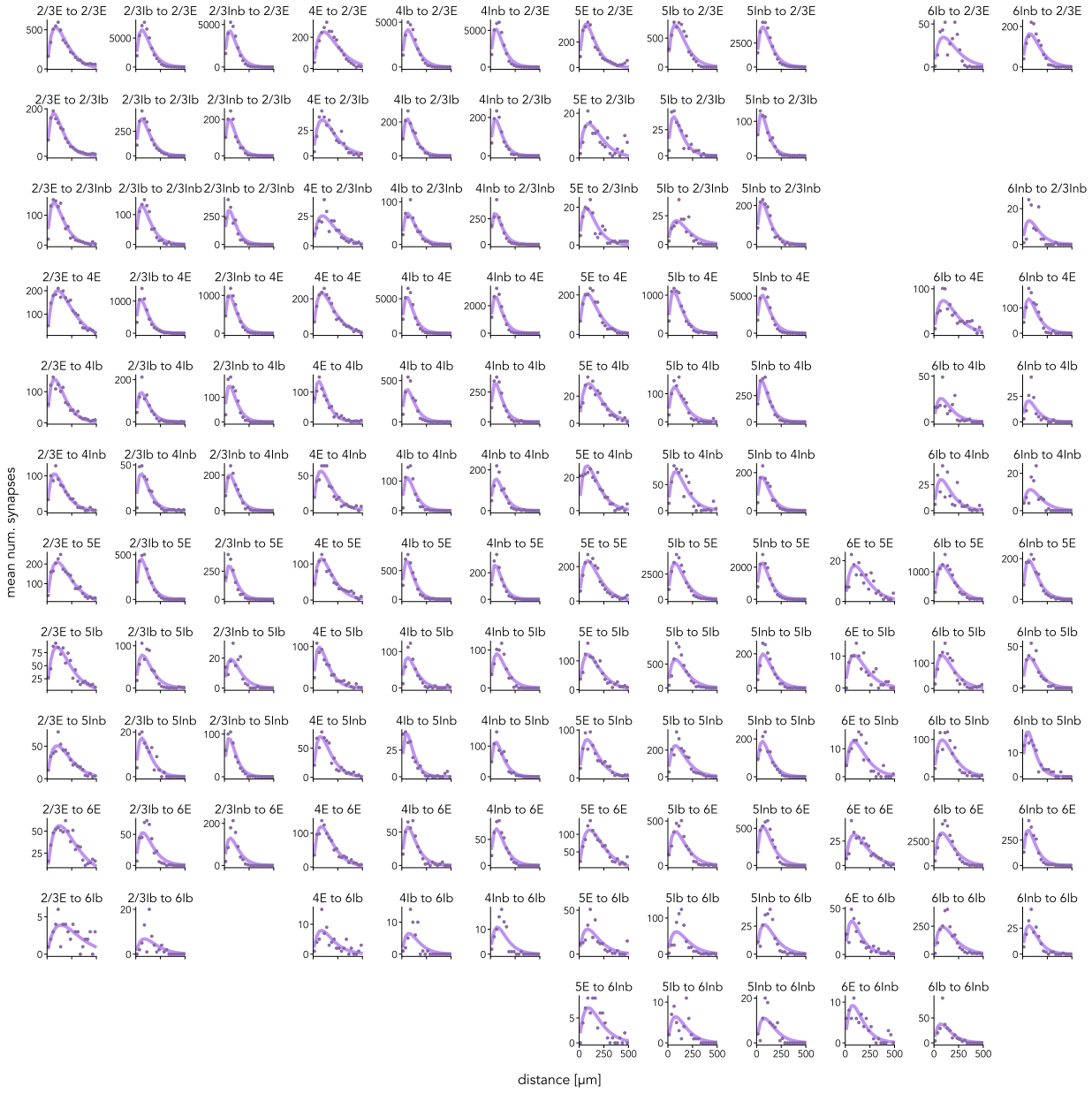

Figure S1: **Density of mean number of synapses between pre- and postsynaptic populations from EM data, actual connectivity.** Purple dots indicate experimentally observed number of connections at distance d, purple curves are fits to the expected number of connections given the density of the mean number of synapses of one presynaptic neuron with all possible partners from the postsynaptic population at distance d (Equation 4). No fits for combinations of populations where the observed number of synapses is smaller than 50.

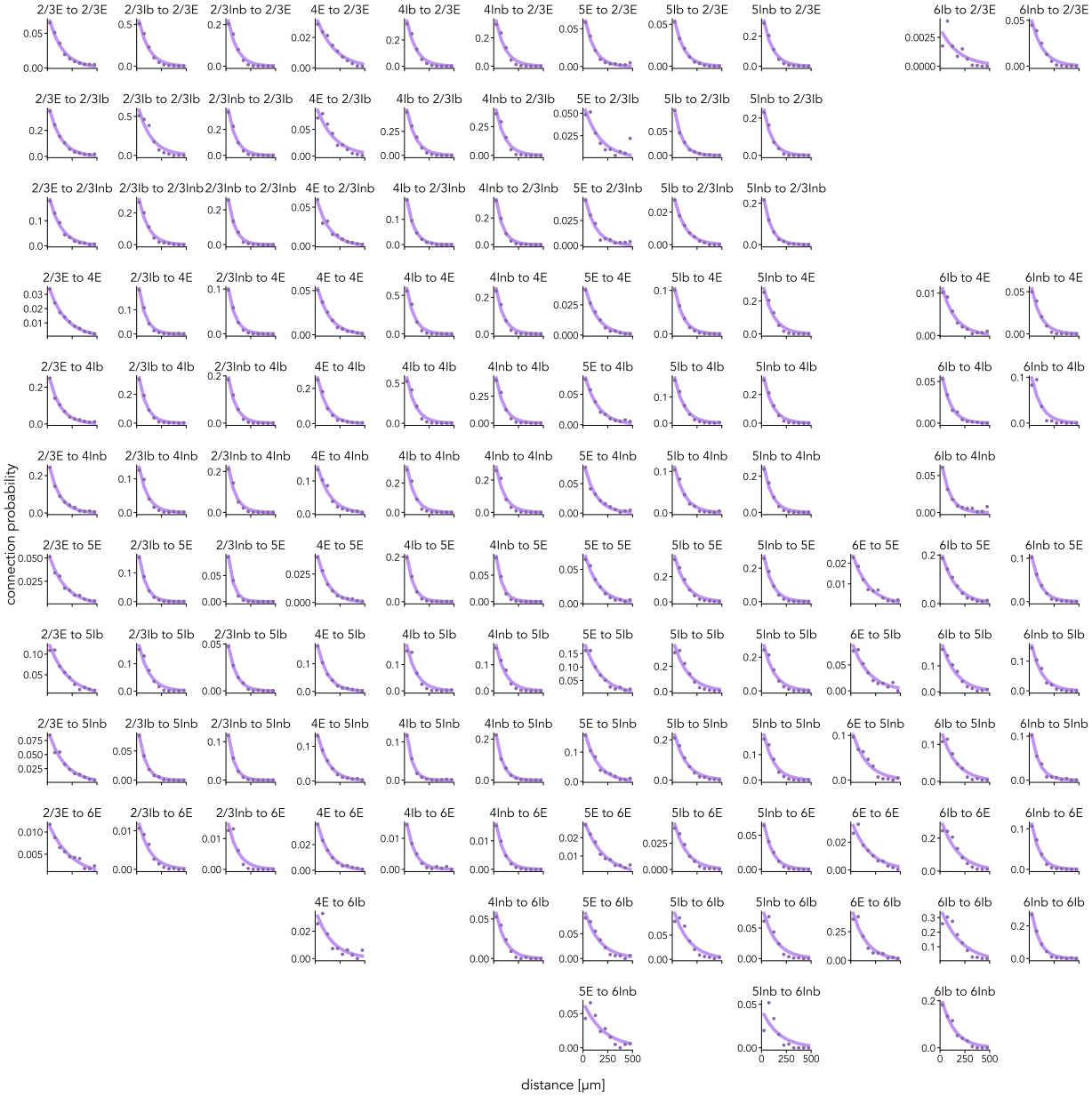

Figure S2: **Connection probability between pre- and postsynaptic populations from EM data, actual connectivity.** Purple dots indicate experimentally observed connection probability at distance d, purple curves are fits to the expected connection probability (Equation 2). No fits for combinations of populations where the observed number of connections is smaller than 50.

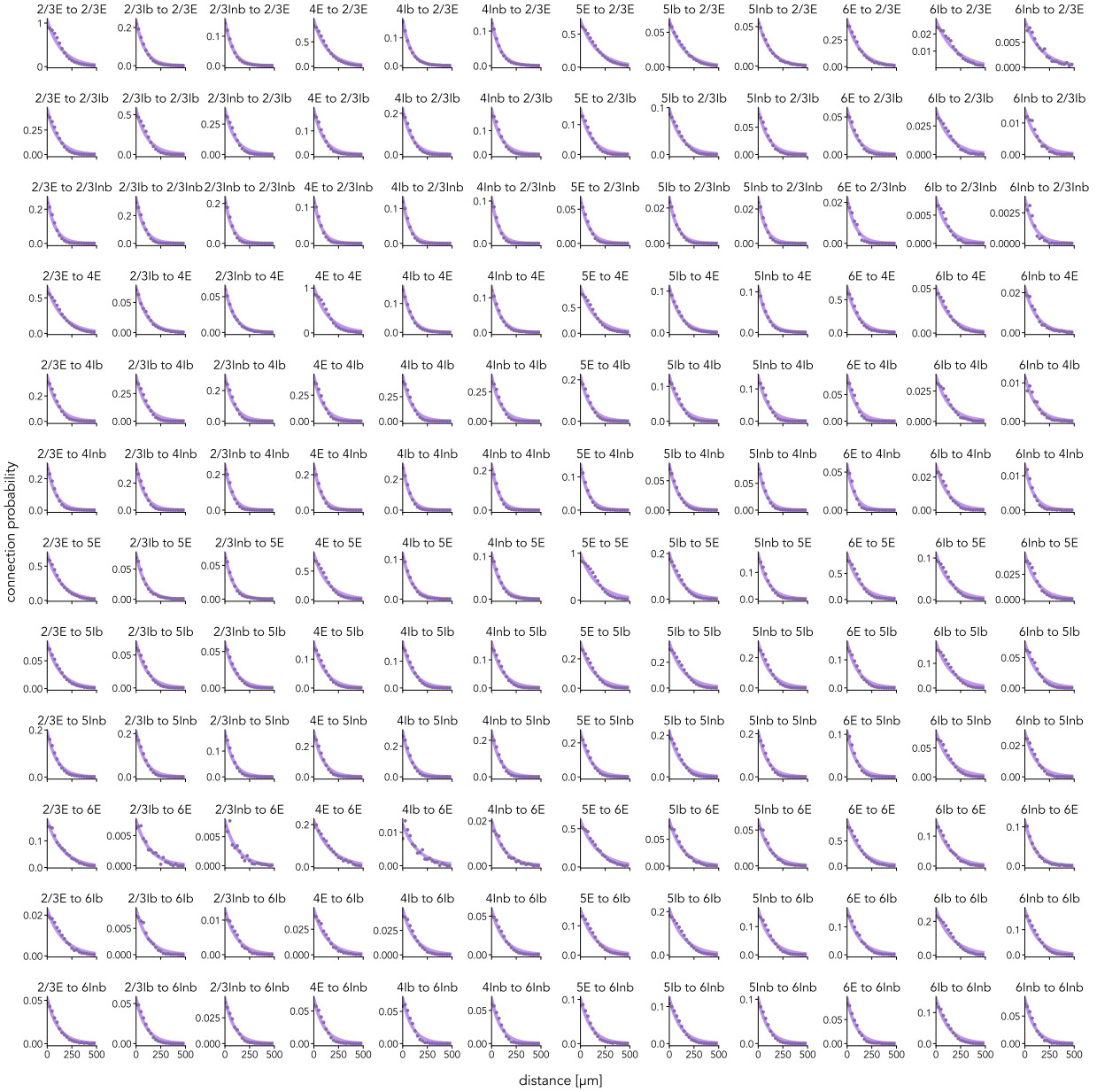

Figure S3: **Connection probability between pre- and postsynaptic populations from EM data, potential connectivity.** Purple dots indicate connection probability at distance d, purple curves are fits to the expected connection probability (Equation 2).

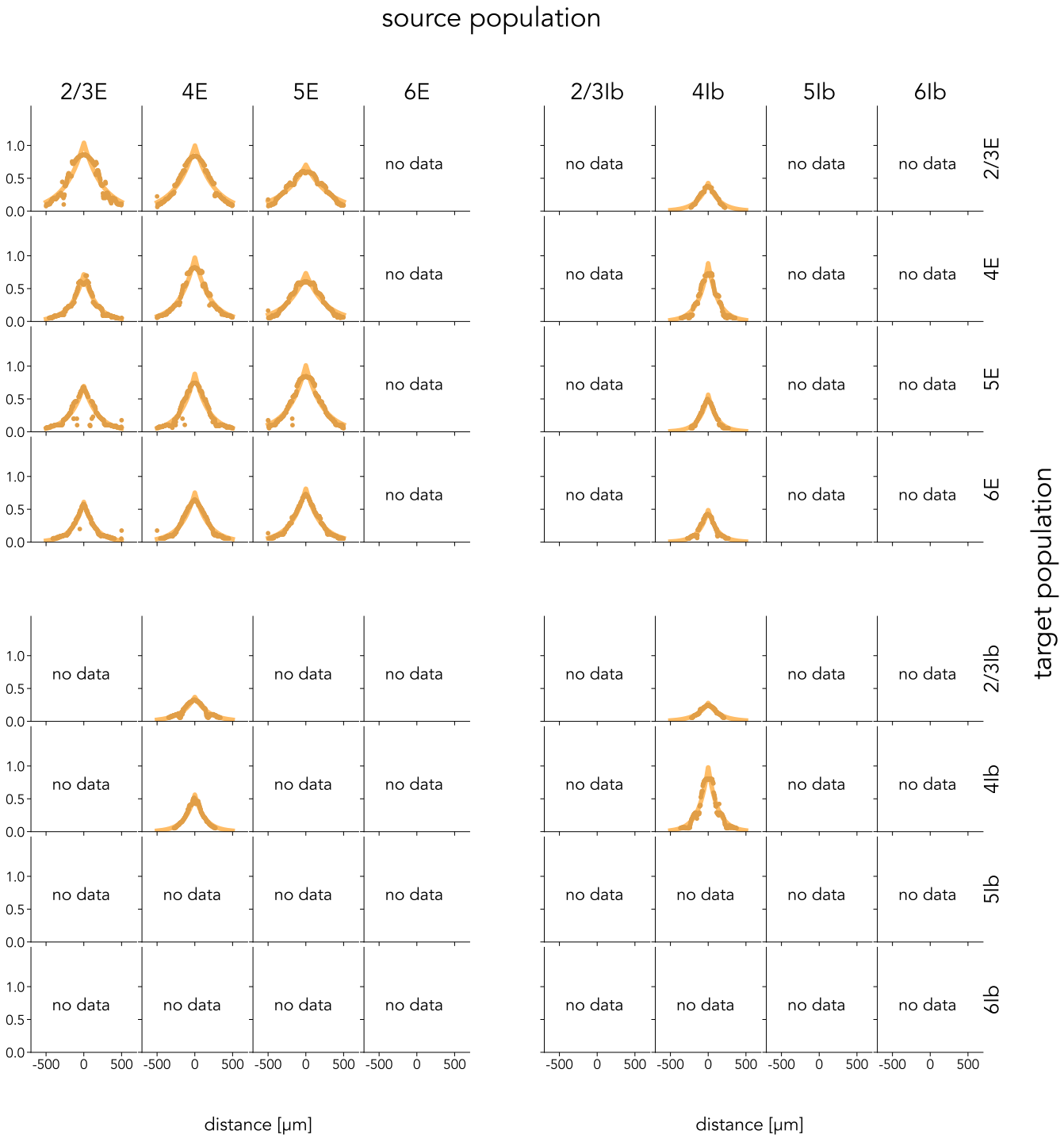

Figure S4: **Potential connectivity between pre- and postsynaptic populations from LM data.** Source population horizontal, target population vertical. Panels show potential connectivity (vertical) at a lateral displacement d as orange dots. Orange curves are fits to the connection probability according to Equation 2 for E-to-E connections, and mean number of synapses according to Equation 1 for all other types of connections.

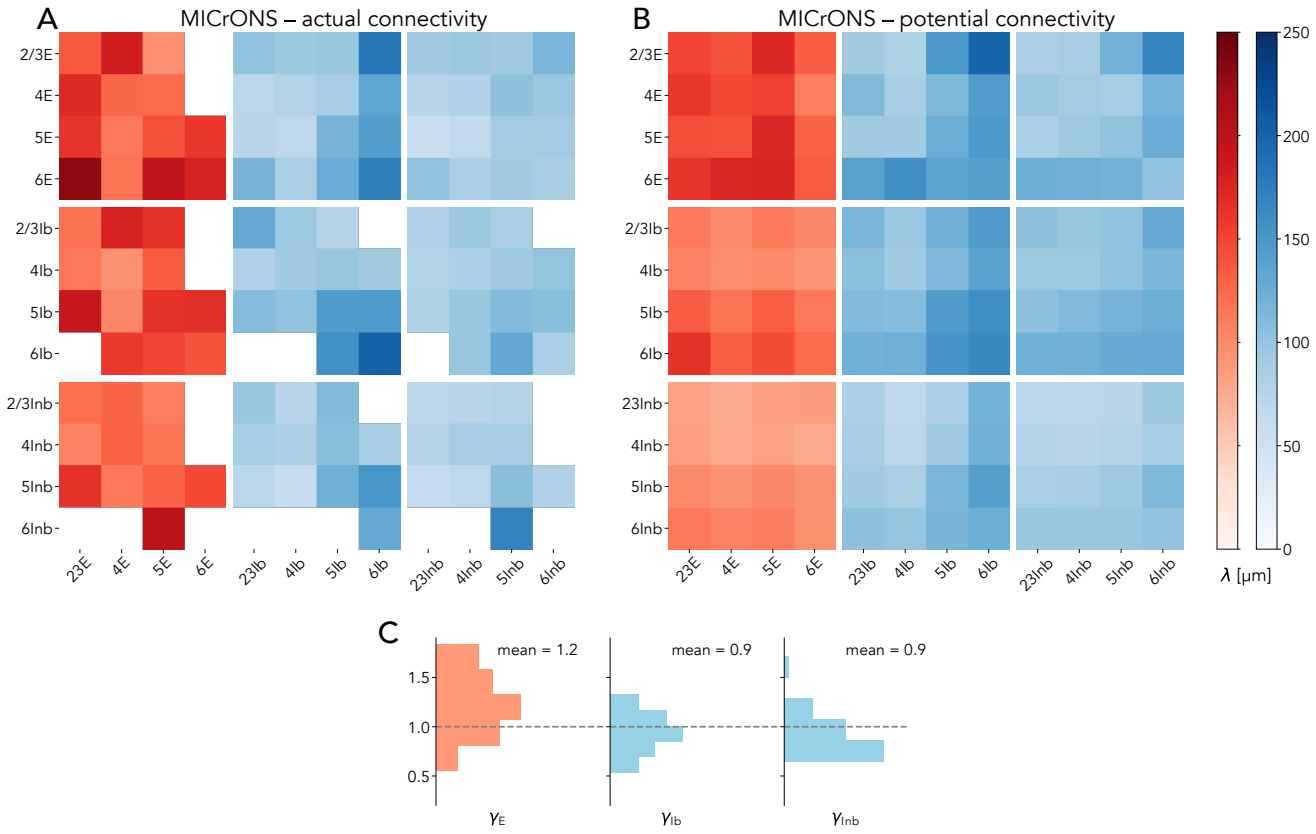

Figure S5: **Comparison of the length scales of connection probability derived from actual and potential connectivity of EM data. A** Characteristic length scale $\lambda_{AB}^{\text{conn}}$ derived from actual connectivity. **B** Characteristic length scale $\lambda_{AB}^{\text{conn,pot}}$ derived from potential connectivity. **C** Fraction of length scales $\gamma_X = \lambda_{A,vX}^{\text{conn}} / \lambda_{A,vX}^{\text{conn,pot}}$ where $X \in \{\text{E}, \text{Ib}, \text{Inb}\}$.

S1.2 Characteristic lengths for $\mathcal{M}_{LM}$

Since the data of Stepanyants et al. [1] do not have the required resolution for the derivation in Section 2.2, we generalize the missing values from the estimated $\lambda^{\text{syn}}_{AB}$. For inhibitory source populations, we choose

$$\lambda^{\text{syn}}_{\text{5Ib,4Ib}} = \lambda^{\text{syn}}_{\text{5E,4Ib}} \tag{12}$$
$$\lambda^{\text{syn}}_{\text{6Ib,4Ib}} = \lambda^{\text{syn}}_{\text{6E,4Ib}} \tag{13}$$
$$\lambda^{\text{syn}}_{A,v\text{Ib}} = \lambda^{\text{syn}}_{A,\text{4Ib}} \tag{14}$$

where A represents any target population, and v represents any source layer. Since Stepanyants et al. [1] only provide data for inhibitory basket cells, we use the same characteristic length scales also for inhibitory non-basket cells.

For excitatory source populations, we choose

$$\lambda^{\text{syn}}_{u\text{Ib},v\text{E}} = \lambda^{\text{syn}}_{u\text{E},v\text{E}} \tag{15}$$

for all source layers except $v = 6$ since data for this layer is lacking. There, we choose

$$\lambda^{\text{syn}}_{A,\text{6E}} = \lambda^{\text{syn}}_{A,\text{5E}} \ , \tag{16}$$

see Table 1.

Characteristic lengths $\lambda^{\text{syn}}_{AB}$ of the mean number of synapses

Target population	**Source population**							
	2/3E	**2/3Ib**	**4E**	**4Ib**	**5E**	**5Ib**	**6E**	**6Ib**
2/3E	171 µm	146 µm	171 µm	146 µm	216 µm	146 µm	216 µm	146 µm
2/3Ib	171 µm	160 µm	179 µm	160 µm	216 µm	160 µm	216 µm	160 µm
4E	115 µm	131 µm	136 µm	131 µm	173 µm	131 µm	173 µm	131 µm
4Ib	115 µm	124 µm	134 µm	124 µm	173 µm	124 µm	173 µm	124 µm
5E	129 µm	117 µm	123 µm	117 µm	154 µm	117 µm	154 µm	117 µm
5Ib	129 µm	117 µm	123 µm	117 µm	154 µm	117 µm	154 µm	117 µm
6E	103 µm	120 µm	123 µm	120 µm	132 µm	120 µm	132 µm	120 µm
6Ib	102 µm	120 µm	123 µm	120 µm	132 µm	120 µm	132 µm	120 µm

Table 1: Characteristic lengths $\lambda^{\text{syn}}_{AB}$ of the mean number of synapses for model $\mathcal{M}_{LM}$. Green values are estimated directly from Stepanyants et al. [1], black values are generalized from these estimates.

S1.3 Connection strengths

We follow Kraynyukova et al. [2] in defining the connection strength J^v_{XY} in a layer v from neurons of population vY to vX as

$$J^v_{XY} = \text{average in-degree to single neuron in } vX \text{ from } vY \times \text{corresponding PSP}.$$

To compare our results with theirs, we only consider inhibitory basket cell populations and discard populations of inhibitory non-basket cells. We find that the weights chosen in the present work (c.f. Section 2.3) satisfy the hierarchy of connection strengths found in Kraynyukova et al. [2] (called connectivity weights in their study) in most cases. Additionally, we display the synaptic weights (assessed by unitary PSPs) used in Kraynyukova et al. [2] originating from previous measurements (their reference Allen Institute for Brain Science, 2019). For these synaptic weights, the hierarchy is satisfied for the EM model in all cases except L6 EI-EE (Figure S7, lower left panel). This is consistent with their findings using connection probabilities in mouse V1 obtained by electrophysiological means (their Figure 4).

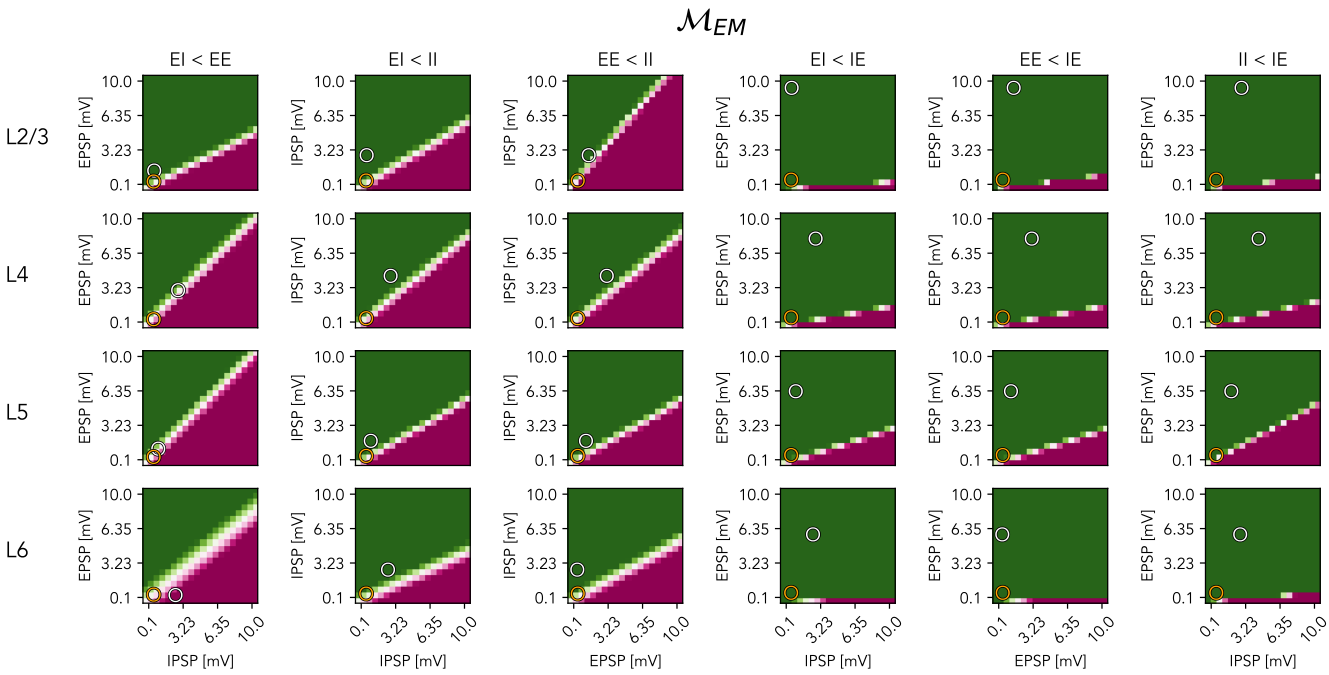

Figure S6: **Connection strengths for $\mathcal{M}_{EM}$.** Layer- and population-pair-resolved connection strengths when systematically varying the PSP of presynaptic populations. On the horizontal (vertical) axis, the PSP of presynaptic populations with putatively smaller (larger) connection strengths is varied. Weights chosen in this work marked in orange, weights by the Allen Institute marked in white. Green (purple) indicates that the inequality given in the column title is fulfilled (unfulfilled) and therefore a hierarchy of connection strengths exists (does not exist).

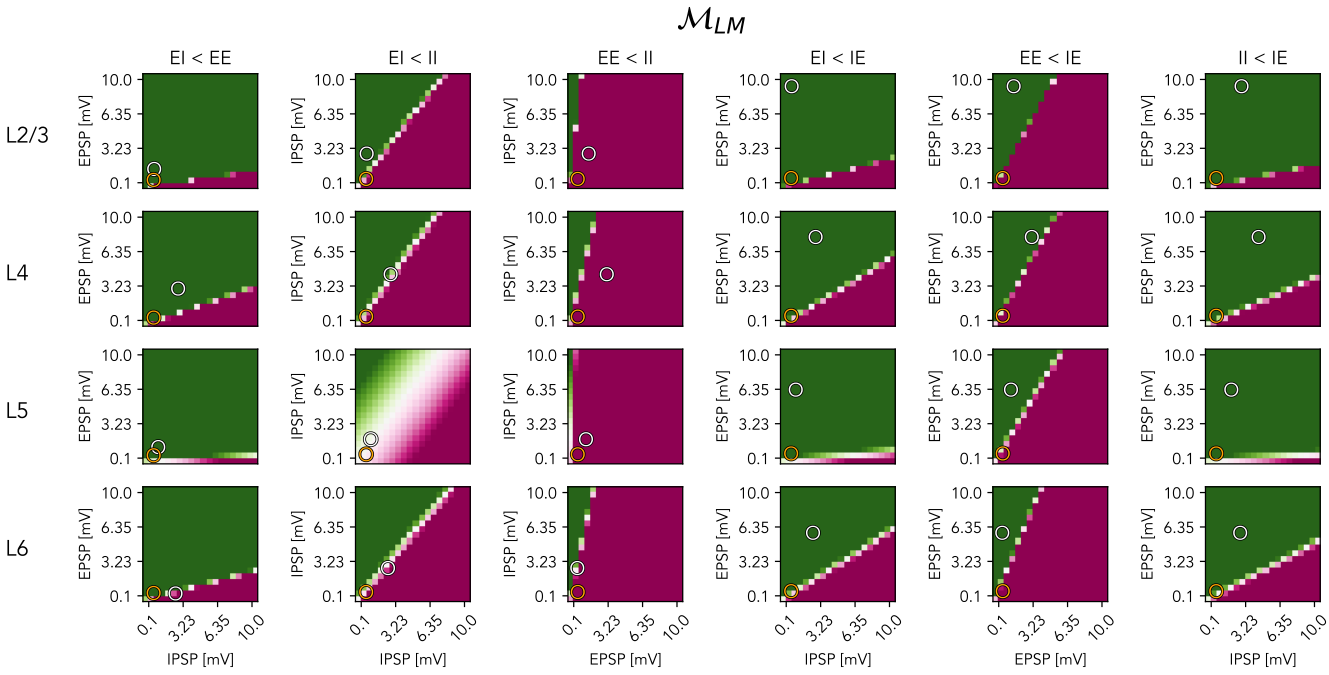

Figure S7: **Connection strengths for $\mathcal{M}_{LM}$.** Same layout and color scheme as in Figure S6.

S1.4 Tables summarizing model definitions

The network architecture and the list of parameters are summarized in the style of Nordlie et al. [3]. Table 2 summarizes the models, Table 3 specifies neuron and synapses models, Table 4, Table 5, and Table 6 give the numeric values used in the simulations.

Structure	Multi-layer network of excitatory, inhibitory basket and non-basket neurons
Populations	12 cortical populations in 4 layers (L2/3, L4, L5, L6), populations vY for all v in layers, $Y \in \{\mathrm{E}, \mathrm{Ib}, \mathrm{Inb}\}$
Measurements	Spikes and membrane potential of neurons in all populations
Neuron Model	Leaky integrate-and-fire neurons, E and Inb neurons with adaptation
Synapse Model	Conductance-based synapses with exponentially shaped kernel
Network Model	Pairwise Bernoulli connectivity rule
External Drive	Modulations of excitatory conductances with an Ornstein-Uhlenbeck process

Table 2: Model summaries for $\mathcal{M}_{LM}$ and $\mathcal{M}_{EM}$

Neuron and synapse model for excitatory and inhibitory non-basket cells	
Sub-threshold dynamics	$C_m\dot{V}_m = -g_L\left(V_m - E_L\right) - \left(g_{\text{ex}} + g_{\text{ext}}\right)\left(V_m - E_{\text{ex}}\right) - g_{\text{in}}\left(V_m - E_{\text{in}}\right)$ $-g_{\text{a}}\left(V_m - E_{\text{a}}\right) - g_{\text{rr}}\left(V_m - E_{\text{rr}}\right)$ $\tau_{\text{ex}}\dot{g_{\text{ex}}}(t) = -g_{\text{ex}}(t) + \tau_{\text{ex}}\sum_j w_j \sum_{t_j}\delta(t - t_j - d_j)$ $\tau_{\text{in}}\dot{g_{\text{in}}}(t) = -g_{\text{in}}(t) + \tau_{\text{in}}\sum_k w_k \sum_{t_k}\delta(t - t_k - d_k)$ $\tau_{\text{a}}\dot{g_{\text{a}}}(t) = -g_{\text{a}}(t) + \tau_{\text{a}}\sum_{t_i}\delta(t - t_i)$ $\tau_{\text{rr}}\dot{g_{\text{a}}}(t) = -g_{\text{rr}}(t) + \tau_{\text{rr}}\sum_{t_i}\delta(t - t_i)$ where t_i is the timing of the spike emitted by the neuron.
Spiking	If $V(t-) < V_{\text{th}}$ and $V(t+) \geq V_{\text{th}}$: 1. Set $t^* = t$ and $V(t) = V_{\text{reset}}$ in $(t^*, t^* + \tau_r]$. 2. Emit spike with time stamp t^*.
Neuron and synapse model for inhibitory basket cells	
Sub-threshold dynamics	$C_m\dot{V}_m = -g_L\left(V_m - E_L\right) - \left(g_{\text{ex}} + g_{\text{ext}}\right)\left(V_m - E_{\text{ex}}\right) - g_{\text{in}}\left(V_m - E_{\text{in}}\right)$ $\tau_{\text{ex}}\dot{g_{\text{ex}}}(t) = -g_{\text{ex}}(t) + \tau_{\text{ex}}\sum_j w_j \sum_{t_j}\delta(t - t_j - d_j)$ $\tau_{\text{in}}\dot{g_{\text{in}}}(t) = -g_{\text{in}}(t) + \tau_{\text{in}}\sum_k w_k \sum_{t_k}\delta(t - t_k - d_k)$
Spiking	If $V(t-) < V_{\text{th}}$ and $V(t+) \geq V_{\text{th}}$: 1. Set $t^* = t$ and $V(t) = V_{\text{reset}}$ in $(t^*, t^* + \tau_r]$. 2. Emit spike with time stamp t^*.
Computation time step	
Time resolution	$\mathrm{d}t = 0.1\,\text{ms}$
Synaptic delays	
Delay	Synaptic delay is exponentially distributed with a mean depending on the pre- and postsynaptic cell type. The minimal synaptic delay equals $\mathrm{d}t$.
Synaptic weights	
Weights	Synaptic weights are lognormally distributed with a fixed relative (to the mean) standard deviation and the mean depending on the pre- and postsynaptic cell type.
Stimulation	
External drive	$\tau_{\text{ext}}\dot{g_{\text{ext}}}(t) = -(g_{\text{ext}}(t) - \mu) + \sigma\sqrt{2\tau_{\text{ext}}}\eta(t)$ where η denotes white noise, μ and σ are population-specific.

Table 3: Neuron and synapse models used for spiking neural network simulations of both $\mathcal{M}_{LM}$ and $\mathcal{M}_{EM}$.

Parameter	Value	Description
Neuron parameters: excitatory neurons		
C_m	250 pF	Membrane capacitance
t_{ref}	2 ms	Refractory period
τ_{ex}	2 ms	Excitatory synaptic time constant
τ_{in}	5 ms	Inhibitory synaptic time constant
τ_X	10 ms	Time constant of Ornstein-Uhlenbeck noise
g_L	16.7 nS	Leak conductance
E_L	−70 mV	Resting potential
E_{in}	−75 mV	Inhibitory reversal potential
E_{ex}	0 mV	Excitatory reversal potential
V_{th}	−50 mV	Threshold
V_{reset}	−60 mV	Reset membrane potential
V_m	−60 mV	Initial membrane potential
Neuron parameters: inhibitory basket neurons		
C_m	250 pF	Membrane capacitance
t_{ref}	4 ms	Refractory period
τ_{ex}	2 ms	Excitatory synaptic time constant
τ_{in}	5 ms	Inhibitory synaptic time constant
τ_X	10 ms	Time constant of Ornstein-Uhlenbeck noise
g_L	16.7 nS	Leak conductance
E_L	−70 mV	Resting potential
E_{in}	−75 mV	Inhibitory reversal potential
E_{ex}	0 mV	Excitatory reversal potential
V_{th}	−50 mV	Threshold
V_{reset}	−60 mV	Reset membrane potential
V_m	−60 mV	Initial membrane potential
Neuron parameters: inhibitory non-basket neurons		
C_m	250 pF	Membrane capacitance
t_{ref}	4 ms	Refractory period
τ_{ex}	2 ms	Excitatory synaptic time constant
τ_{in}	5 ms	Inhibitory synaptic time constant
τ_X	10 ms	Time constant of Ornstein-Uhlenbeck noise
g_L	16.7 nS	Leak conductance
E_L	−65 mV	Resting potential
E_{in}	−75 mV	Inhibitory reversal potential
E_{ex}	0 mV	Excitatory reversal potential
V_{th}	−50 mV	Threshold
V_{reset}	−60 mV	Reset membrane potential
V_m	−60 mV	Initial membrane potential
Adaptation parameters		
q_{sfa}	14.48 nS	Quantal spike-frequency adaptation conductance increase
q_{rr}	3214 nS	Quantal relative refractory conductance increase
τ_{sfa}	110 ms	Time constant of spike-frequency adaptation
τ_{rr}	1.97 ms	Time constant of relative refractoriness
E_{sfa}	−70 mV	Spike-frequency reversal potential
E_{rr}	−70 mV	Relative refractory reversal potential

Table 4: Neuron parameters for both $\mathcal{M}_{LM}$ and $\mathcal{M}_{EM}$.

Mean delay

Target cell type	Source cell type		
	E	**Ib**	**Inb**
E	2 ms	0.8 ms	1.5 ms
Ib	1.2 ms	1.5 ms	1.5 ms
Inb	1.5 ms	1.2 ms	1.5 ms

Table 5: Mean delays between populations of given cell types for both $\mathcal{M}_{LM}$ and $\mathcal{M}_{EM}$. Numerical values inspired by measurements from Avermann et al. [4].

Mean connection weights

Target cell type	Source cell type		
	E	**Ib**	**Inb**
E	0.4 nS	4.7 nS	4.0 nS
Ib	0.8 nS	4.7 nS	3.2 nS
Inb	0.4 nS	6.5 nS	4.0 nS

Table 6: Mean connection weights between populations of given cell type for both $\mathcal{M}_{LM}$ and $\mathcal{M}_{EM}$. Numerical values inspired by measurements from Avermann et al. [4]. Relative standard deviation of weights equals 0.5.

μ_X **for** $\mathcal{M}_{LM}$

Layer	Cell type		
	E	**Ib**	**Inb**
L2/3	6.34 nS	6.79 nS	5.78 nS
L4	8.07 nS	6.67 nS	5.57 nS
L5	6.79 nS	5.61 nS	5.66 nS
L6	8.00 nS	9.12 nS	8.22 nS

Table 7: Mean of conductance fluctuations modeled as OU processes providing external drive for the tuned $\mathcal{M}_{LM}$ network.

μ_X **for** $\mathcal{M}_{EM}$

Layer	Cell type		
	E	**Ib**	**Inb**
L2/3	7.29 nS	6.55 nS	4.50 nS
L4	7.85 nS	8.45 nS	5.72 nS
L5	11.98 nS	11.54 nS	7.58 nS
L6	5.60 nS	5.45 nS	3.94 nS

Table 8: Mean of conductance fluctuations modeled as OU processes providing external drive for the tuned $\mathcal{M}_{EM}$ network.

References

[1] A. Stepanyants et al. "Local Potential Connectivity in Cat Primary Visual Cortex". *Cerebral Cortex* 18.1 (2007), pp. 13–28.

[2] N. Kraynyukova et al. "In vivo extracellular recordings of thalamic and cortical visual responses reveal V1 connectivity rules". *Proceedings of the National Academy of Sciences of the United States of America* 119.41 (2022), e2207032119.

[3] E. Nordlie, M.-O. Gewaltig, and H. E. Plesser. "Towards Reproducible Descriptions of Neuronal Network Models". *PLOS Computational Biology* 5.8 (2009), e1000456.

[4] M Avermann et al. "Microcircuits of excitatory and inhibitory neurons in layer 2/3 of mouse barrel cortex". *Journal of Neurophysiology* 107.11 (2012), pp. 3116–3134.